Propagation of Swift Protons in Liquid Water and Generation of Secondary Electrons in Biomaterials

Pablo de Vera, Rafael Garcia-Molina and Isabel Abril

Abstract A proper description of the propagation of a swift proton beam through biomaterials, accounting for the energy deposited as well as the geometrical evolution of the beam as a function of the target depth and nature, is a crucial issue in proton therapy. For this purpose, simulation is a very adequate tool, since the most relevant interactions that take place between the projectile and the target constituents (electrons and nuclei) can be conveniently accounted for in a controlled manner. In this chapter an overview and relevant results for hadron therapy are presented of the simulations we have developed using the code SEICS (Simulation of Energetic Ions and Clusters through Solids), which combines Monte Carlo and Molecular Dynamics, to follow in detail the motion and energy deposition of swift protons through targets of hadron therapeutic interest, mainly liquid water. The main interactions considered in our study are of elastic nature (affecting mainly the projectile's direction) and inelastic processes (leading to either nuclear reactions or electronic energy loss). The performance of the code, as well as the quality of its main input, namely the stopping force for proton beams in liquid water (which is the main tissue constituent), are benchmarked by comparing the results of the simulations with available experimental proton energy spectra as a function of the detection angle after traversing a

P. de Vera
Department of Physical Sciences, The Open University,
Milton Keynes, England MK7 6AA, UK
e-mail: p.devera@qub.ac.uk

P. de Vera
MBN Research Center, 60438 Frankfurt am Main, Germany

P. de Vera
School of Mathematics and Physics, Queen's University Belfast,
BT7 1NN Belfast, Northern Ireland, UK

R. Garcia-Molina (✉)
Departamento de Física – Centro de Investigación en Óptica y Nanofísica,
Regional Campus of International Excellence "Campus Mare Nostrum",
Universidad de Murcia, 30100 Murcia, Spain
e-mail: rgm@um.es

I. Abril
Departament de Física Aplicada, Universitat d'Alacant, 03080 Alacant, Spain

© Springer International Publishing Switzerland 2017

A.V. Solov'yov (ed.), *Nanoscale Insights into Ion-Beam Cancer Therapy*,
DOI 10.1007/978-3-319-43030-0_2

micrometric liquid water jet. The excellent agreement with experiments validates the SEICS code, which we can use then to study several problems of interest for proton therapy, including the calculation of depth-dose curves and lateral dose profiles, the energy evolution of the proton beam along the target, as well as the production of secondary electrons at the Bragg peak in relevant biomaterials.

1 Introduction

The interaction of fast charged particles with biological materials is a topic of great current interest, due to its possible (beneficial or harmful) consequences on human tissues. The passage of energetic ions through the body initiates a cascade of physical, chemical and biological processes, which can produce the damage and, eventually, the death, of human cells. Such results can be considered either as negative (when the damage should be prevented) or positive (when it is desired), so a proper description and understanding of the involved phenomena is desirable, in each case, for radiation protection or for radiotherapeutic purposes.

While radiation protection against energetic ions is relevant to prevent human exposure in the context of nuclear reactors and space exploration, radiotherapeutic purposes find an emergent application in the technique known as ion beam cancer therapy (or hadron therapy) [1]. Contrary to conventional radiotherapy, where energetic photon or electron beams are used, having a rather homogeneous energy deposition profile in human tissues, ion beam cancer therapy exploits the unique characteristics of energetic ion beams, which present an inverse depth-dose profile, losing more energy as their kinetic energy decreases. This behaviour gives place to the appearance of the Bragg peak, i.e., a sharp maximum in the energy deposition profile near the end of the trajectories of the energetic ions. The depth (in the target) of the Bragg peak has to be carefully tuned. For that purpose, it is necessary to improve the knowledge of the interaction processes that take place when swift ion beams move through biological materials. This will allow a precise energy delivery in deep-seated tumours, while minimising the damage to surrounding healthy tissues, which is especially desirable for treating tumours close to sensitive areas, such as the brain. For ion beam cancer therapy, usually proton and carbon ion beams are used, although the majority of centres all around the world employ protons [2].

Energetic ions moving through condensed matter (solids and liquids) lose energy mainly by electronic excitations and ionisations. The main quantity describing this energy loss is the stopping power (or stopping force) [3]. Its accurate determination for biological materials and, especially, for liquid water (the main constituent of living tissues) is an important issue, since it will determine the precision with which the Bragg peak can be positioned and, hence, the accuracy of treatment plannings [4, 5]. However, electronic excitation and ionisation are just two of the multiple phenomena which occur since the ion begins its propagation in the body until the final biological damage.

Ion beam cancer therapy should be studied, indeed, within a multiscale approach [6], since processes in very different energy, spatial, and time scales take place.

Apart from electronic interactions, ion propagation is influenced by nuclear fragmentation reactions, which convert the initial projectiles in a new whole family of propagating secondary particles. The electronic interactions lead to the ejection of a vast quantity of secondary species, including secondary electrons and free radicals, which propagate in nano- and micrometric scales, inducing the physical and chemical mechanisms that account for the major part of the initial damage of the biomolecules, especially the nuclear DNA. Then, biological processes come into play, dealing with the damage and reparation of the biomolecules, which will lead to cell death if the latter mechanism is not effective.

Therefore, it is clear that an optimal use of ion beam cancer therapy requires knowledge on multiple phenomena, among which, from the physics point of view, electronic excitation and ionisation, and nuclear fragmentation reactions, play a relevant role. A convenient way of modelling ion beam interaction with biological materials, taking into account all these physical interactions, is numerical simulation, such as Monte Carlo and Molecular Dynamics. In the Monte Carlo codes, the detailed history of each projectile of the beam is followed by randomly drawing the coordinate at which each possible interaction (elastic or inelastic scattering, electron exchange between the projectile and the target, nuclear fragmentation reaction...) takes place, as well as the final result of the interaction, by using appropriate interaction probabilities, known as cross sections.

Depending on the kind of code, more or less detailed information will be obtained from the simulation. Track-structure (or event by event) codes are the most complete ones, in which the result of each interaction is described and followed in detail. This is particularly important for the emission of secondary electrons: in the track-structure codes, the energy and angle of each secondary electron is determined after each ionising collision, and then the electrons are also followed until stopped. Examples of such codes are KURBUC [7], PARTRAC [8], NOTRE DAME [9], MC4 [10], and EPOTRAN [11], among others [10].

As a consequence of being very detailed, these simulations are also very time consuming, and not very convenient when only macroscopic dose distributions are needed. In those cases, radiation transport (or condensed history) codes can be used, by grouping bunches of interactions that, by themselves, have a small effect on the projectile history, which greatly reduce computational time. This is done, for example, with the electronic interactions when the trajectories of the secondary electrons are not important, i.e., for the calculation of macroscopic dose profiles. Some examples of condensed history codes are FLUKA [12], MCNPX [13], SRIM [14], PENELOPE [15] or GEANT4 [16], among others [17]. Also, codes exist that can use the condensed history algorithm for the whole target, while calculating the track-structure just for the regions of interest, such as GEANT4-DNA [18] or LEPTS [19, 20], which enable more efficient multiscale simulations.

However, in order to obtain proper results from Monte Carlo codes, they have to be fed with appropriate input, i.e., with accurate values of the cross sections for each interaction process, notably for the electronic excitation in condensed phase targets, such as liquid water. In this context, the code SEICS (Simulation of Energetic Ions and Clusters through Solids) has been developed over the last years, for the description

of swift ion propagation through a target by taking special care on its condensed matter nature [21]. The SEICS code employs accurate electronic stopping quantities, obtained from the dielectric formalism [22], by properly taking into account the stochastic energy loss of swift ions in condensed organic targets, such as liquid water [23], bone [24] or other biotargets [25–28]. Therefore, this code represents a good tool for the simulation of ion beam interactions with biomaterials.

The SEICS code will be briefly described in Sect. 2. After some initial considerations on the way the code works, in Sect. 2.1 we will explain in detail how the electronic energy loss of proton beams in liquid water is calculated, taking into account the stochasticity of the process through the use of the stopping power and the energy-loss straggling, as well as the charge state of the projectile. Then, the rest of relevant interactions in the problem will be described, namely elastic scattering (Sect. 2.2), electron capture and loss processes (Sect. 2.3), and nuclear fragmentation reactions (Sect. 2.4). In particular, we will show how, even recognizing the complexity of nuclear fragmentation reactions, they can be implemented in a quite simple way for proton beams.

After describing the code, and before studying several problems related to proton therapy, in Sect. 3 we will benchmark both the code and its main input, i.e., the electronic stopping quantities for protons in liquid water. This will be done by comparing the outputs from SEICS with the results of the experiments performed in micrometric liquid water jets by the Kyoto group [29, 30], which were done to determine the stopping power of liquid water for proton beams of intermediate energy. The excellent agreement of our simulated energy distributions with the corresponding measurements validate the performance of our code, as well as the accuracy of the stopping quantities we use.

Finally, several applications of the SEICS code to calculate useful quantities in proton therapy are presented in Sect. 4. We will start by calculating depth-dose curves of proton beams in liquid water, Sect. 4.1. Apart from the satisfactory comparison with available experimental data, we will see how the SEICS code can be used to evaluate the contribution of each individual interaction process (electronic energy-loss and straggling, elastic scattering, nuclear fragmentation reactions) to the total dose deposited in the target. Then, in Sect. 4.2 the depth-dose curves will be complemented with the calculation of lateral dose profiles. Here, the simulation results for the lateral aperture of the beam will be parameterised, which yields useful results for the analytical calculations of dose profiles. The energy distribution of protons along the Bragg curve will be discussed in Sect. 4.3, where important characteristics of the energy spectra of primary projectiles along the beam trajectory will be featured. This discussion is very relevant, since the energy distribution of primary projectiles governs the production of secondary electrons, which in turn will determine the microscopic track-structure of the incident radiation. In Sect. 4.4 we will discuss the generalisation of the dielectric formalism to obtain energy spectra of secondary electrons produced by proton beams, and we will use them, in conjunction with the energy distribution of the primary protons as a function of the depth, to determine the realistic energy distributions of secondary electrons produced at the Bragg peak region. Such results are useful to establish the initial conditions for track-structure

simulations in realistic circumstances, where ultimate cellular damage is expected to depend on the number and energy of electrons produced around the Bragg peak region in several relevant biomaterials [31, 32].

2 Propagation of Energetic Ions Through Condensed Media

In order to properly describe the propagation of energetic ions through condensed media, we use the simulation code SEICS (Simulation of Energetic Ions and Clusters through Solids), which is based on a combination of Molecular Dynamics and Monte Carlo techniques to follow the motion of swift projectiles through the target [21, 33–35]. The code implements all the relevant interactions between ions and the target constituents, which are described in what follows. The energy loss by the projectile is mainly due to the electronic excitations and ionisations that it generates along its trajectory, which is accounted for by solving the projectile's equation of motion by considering a stopping force (obtained from the stopping power, i.e., the average energy loss per unit path length) whose fluctuations, due to the stochastic nature of the interaction, are accounted for by the energy-loss straggling; due to the high energies typically used in hadron therapy, relativistic corrections have been included in the kinematics of the projectiles. The multiple Coulomb scattering of the projectile with the target nuclei is the major responsible for the beam angular spreading. The electron capture and loss processes by the projectile determine its charge state, which, in turn, determines the stopping force. Finally, the nuclear fragmentation reactions modify the number of projectiles in the beam and generate new ones, affecting the general shape of the Bragg curve.

Whereas the slowing down of the projectile is managed through a standard Molecular Dynamics procedure, the rest of the processes are drawn by the Monte Carlo technique, where the probability distributions are obtained from the corresponding cross sections.

Besides, an effort has been made to have a more realistic description of the electronic excitation spectrum of the more relevant biological targets, putting especial interest in liquid water, as it is the main constituent of the living tissues, as well as the DNA molecular constituents.

Taking into account all the ingredients cited previously, the SEICS code dynamically follows the trajectory of each projectile in the target, providing its position, velocity and charge-state at any instant. The position $\mathbf{r}$ and velocity $\mathbf{v}$ of a projectile, with mass M_1 and atomic number Z_1, are obtained by numerically solving its equation of motion at discrete time intervals Δt. For this purpose we rewrite the velocity variant of Verlet's algorithm [36], taking into account the relativistic velocities of the projectiles:

$$\mathbf{r}(t+\Delta t) = \mathbf{r}(t) + \mathbf{v}(t)\Delta t + \frac{\mathbf{F}(t)}{2M_1}(\Delta t)^2 \left[1 - \left(\frac{v(t)}{c}\right)^2\right]^{3/2}, \quad (1)$$

$$\mathbf{v}(t+\Delta t) = \mathbf{v}(t) + \frac{\mathbf{F}(t) + \mathbf{F}(t+\Delta t)}{2M_1}\Delta t \left[1 - \left(\frac{v(t)}{c}\right)^2\right]^{3/2}, \quad (2)$$

where $\mathbf{F}$ is the electronic stopping force, and c is the speed of light. The classical trajectory of the projectile is followed until it reaches a threshold energy $E_{\rm th}$. We use $E_{\rm th} \sim 250$ eV, although reducing this value has not practical consequences in the final depth-dose distributions.

The force that acts on the projectile is due to its inelastic collisions with the target electrons. This produces the so-called electronic stopping force, which depends on the projectile charge-state q and speed v. Due to the stochastic nature of the interaction with the target electrons there are fluctuations in the force sensed by the projectile. Then, in the simulation we use the modulus of the electronic stopping force felt by the projectile (with charge state q) from a Gaussian distribution with mean value S_q (the stopping power or mean value of the energy loss), and a standard deviation given by:

$$\sigma = \sqrt{\Omega_q^2/\Delta s}\,, \quad (3)$$

where $\Delta s = v\Delta t$ is the distance travelled by the projectile (with velocity v) in a time step Δt, and Ω_q^2 is the energy-loss straggling (the mean square deviation per unit path length of the energy-loss distribution) for a projectile with charge state q. According to the Box-Müller procedure to generate a Gaussian distribution [37], the electronic stopping force acting on the projectile is written as:

$$\mathbf{F} = -\left[S_q + (\Omega_q/\sqrt{\Delta s})\sqrt{-2\ln\xi_1}\cos(2\pi\xi_2)\right]\hat{v}\,, \quad (4)$$

with $\hat{v}$ being the unit vector of the instantaneous projectile velocity $\mathbf{v}$. The symbols ξ_i refer to random numbers uniformly distributed between 0 and 1 [38], with the value of the subscript i (= 1, 2, ...,) denoting each time a random number ξ_i is used in the simulation.

The stopping power S_q and the energy-loss straggling Ω_q^2 of the projectile are the main input quantities in the simulation code. They are calculated in the dielectric framework, together with the MELF-GOS (Mermin Energy Loss Function – Generalised Oscillator Strength) model [39, 40], which has been developed to realistically represent the electronic excitation spectrum of any condensed media, being particularly convenient for biological targets, which are liquids or solids [25, 41]. To speed up the simulation, at higher projectile velocities ($v \geq 20$ a.u.; kinetic energies $T \geq 10$ MeV/u) we use the analytical relativistic Bethe formula for the stopping power [42],

$$S = \frac{4\pi e^4 Z_2 Z_1^2 \mathscr{N}}{v^2} \ln\left[\frac{2mv^2}{I(1-(v/c)^2)} - (v/c)^2\right], \tag{5}$$

where Z_2 is the atomic number of the target, $\mathscr{N}$ is its atomic or molecular density, m and e are the electron mass and charge, respectively, and I is the mean excitation energy of the target, which only depends on its electronic structure [43], and it is found from the MELF-GOS model [25, 44]. Also at high energies, the energy-loss straggling Ω_q^2 is evaluated from the Bohr straggling formula [3]:

$$\Omega^2_{\text{Bohr}} = 4\pi e^4 Z_2 Z_1^2 \mathscr{N}. \tag{6}$$

The SEICS code becomes a convenient tool to address different problems related to ion beam cancer therapy, since the propagation and energy deposition of the ions through liquid water and other biologically relevant targets can be described with high accuracy.

Althought a complete description of the SEICS code can be found in Refs. [21, 35], in what follows we summarise how the different interactions between a swift charged particle and the target constituents are implemented in it.

2.1 Inelastic Energy Loss Processes

The dielectric formalism is a convenient approach for describing the interaction of fast charged particles with the electrons of a condensed target [22, 45, 46]. It assumes a linear response of the electronic system to the perturbation induced by the electric field of the projectile, providing a connection between the dielectric function of the target (a macroscopic property) and the matrix elements of the electronic transitions (a microscopic quantity). In this case, all the possible electronic excitations of the system are properly accounted for, including many-body and physical-state effects coming from intermolecular interactions, so important in condensed matter.

For an ion with atomic number Z_1, mass M_1 and charge state q, which travels with kinetic energy T (velocity v) through a condensed medium characterised by a dielectric function $\varepsilon(k, \omega)$, the dielectric formalism provides the different moments of the energy-loss distribution due to inelastic collisions of the projectile with the target electrons. The stopping power S_q is given by the first moment of the distribution:

$$S_q(T) = \frac{M_1 e^2}{\hbar\pi T} \int_{\omega_-}^{\omega_+} \mathrm{d}\omega\, (\hbar\omega) \int_{k_-}^{k_+} \frac{\mathrm{d}k}{k} [Z_1 - \rho_q(k)]^2 \mathrm{Im}\left[\frac{-1}{\varepsilon(k,\omega)}\right], \tag{7}$$

where $\hbar k$ and $\hbar\omega$ represent, respectively, the momentum and energy transferred to the target in an inelastic collision. $\rho_q(k)$ is the Fourier transform of the electronic density of the projectile, which is described by the statistical model proposed by Brandt and Kitagawa [47]. The integration limits are $\hbar k_\pm = \sqrt{2M_1\left(2T - \hbar\omega \pm 2\sqrt{T(T-\hbar\omega)}\right)}$,

whereas $\hbar\omega_- = 0$ (for metals) or $\hbar\omega_- = E_{\rm gap}$ (for insulators) and $\hbar\omega_+ \simeq 4Tm/M_1$, where m is the electron mass.

The energy-loss straggling, Ω_q^2, which accounts for fluctuations in the energy loss due to the stochastic nature of the inelastic collisions, is related to the second moment of the distribution. It can be obtained from the following expression:

$$\Omega_q^2(T) = \frac{M_1 e^2}{\hbar\pi T}\int_{\omega_-}^{\omega_+} {\rm d}\omega\,(\hbar\omega)^2 \int_{k_-}^{k_+}\frac{{\rm d}k}{k}[Z_1 - \rho_q(k)]^2 {\rm Im}\left[\frac{-1}{\varepsilon(k,\omega)}\right]. \tag{8}$$

The Brandt-Kitagawa model presupposes that the cloud of bound electrons is screening the projectile nucleus over a certain radius that depends on the projectile velocity. Therefore, target electrons that approach the projectile with impact parameters larger than this radius (that is, distant collisions) perceive the projectile as a point charge with charge q, irrespective of its internal structure. However, when the impact parameter is smaller than the radius (i.e., close collisions) the target electrons penetrate the screening cloud of the bound electrons of the projectile, sensing a partially screened potential corresponding to a projectile charge larger than q. An average over all the impact parameters will give the charge of the projectile. The advantage of this model is that it is possible to derive analytical expressions for the Fourier transform of the electronic charge density of the projectile, $\rho_q(k)$. For more details about the implementation of this model in the SEICS code see Ref. [28].

In Eq. (7) the target properties enter through the energy loss function (ELF), ${\rm Im}[-1/\varepsilon(k,\omega)]$, which characterises the electronic excitation spectrum of the material, since it expresses the probability of producing a target excitation or ionisation with energy and momentum transfers $\hbar\omega$ and $\hbar k$, respectively. A good description of the target ELF at any energy and momentum transfer, the so-called Bethe surface, is basic to obtain accurate values of the stopping power.

On the other hand, the electric field, $\mathscr{E}_{{\rm ind},q}$, induced by the projectile with charge q in the target, which is the responsible of its stopping, can also distort the electronic cloud of the projectile, polarising it. The contribution of this process to the stopping power is given by [34, 48]:

$$S_{{\rm pol},q}(T) = \frac{e^2 M_1 Z_1}{\pi T}\int_{k_-}^{k_+}\frac{{\rm d}k}{k}\rho_q(k)\int_{\omega_-}^{\omega_+}{\rm d}\omega\,\omega\,{\rm Im}\left[\frac{-1}{\varepsilon(k,\omega)}\right]\left[1-\cos\left(\omega d_q\sqrt{\frac{M_1}{2T}}\right)\right]. \tag{9}$$

Here, $d_q = \mu_q \mathscr{E}_{{\rm ind},q}(T)$ is the displacement of the centre of the electron cloud from its nucleus, where μ_q is the projectile polarisability; the self-induced electric field is given by:

$$\mathscr{E}_{{\rm ind},q}(T) = \frac{M_1 e}{\pi T}\int_{k_-}^{k_+}\frac{{\rm d}k}{k}[Z_1 - \rho_q(k)]\int_{\omega_-}^{\omega_+}{\rm d}\omega\,\omega\,{\rm Im}\left[\frac{-1}{\varepsilon(k,\omega)}\right]. \tag{10}$$

This extra contribution to the energy loss of the projectile due to its self-polarisation is also included in the SEICS code.

At this point the only quantity that remains to be determined is the energy loss function of the target at any energy and momentum transfer, that is over the whole Bethe surface, which is not a trivial task. Most of the experiments can measure the ELF at the optical limit ($k = 0$), therefore it is necessary to use methodologies for a proper extension over the whole momentum plane ($k \neq 0$). A discussion about the different extended optical data models currently used to calculate the ELF at any momentum transfers can be found in [41]. In what follows, we will present the MELF-GOS methodology developed by our research group to describe the target ELF over the Bethe surface.

2.1.1 Target Description: The MELF-GOS Model

The MELF-GOS (Mermin Energy Loss Function-Generalised Oscillator Strength) methodology is based on the use of Mermin dielectric functions [49] for the description of the outer-shell electron excitations, together with generalised oscillator strengths in the hydrogenic approach [50] for the description of the inner-shell electron excitations.

Due to the different response to the perturbation induced by the projectile of either the tight-bound outer shell or the inner-shell electrons, the description of both contributions to the ELF can be safely assumed to be independent. Therefore the ELF can be divided in two components:

$$\mathrm{Im}\left[\frac{-1}{\varepsilon\,(k,\omega)}\right] = \mathrm{Im}\left[\frac{-1}{\varepsilon\,(k,\omega)}\right]_{\mathrm{outer}} + \mathrm{Im}\left[\frac{-1}{\varepsilon\,(k,\omega)}\right]_{\mathrm{inner}} . \tag{11}$$

The inner-shell electron excitations present large binding energies, preserving their atomic character and they do not participate in the chemical bonds of the target. Therefore, they can be regarded practically as atomic electrons, being properly described by the generalised oscillator strength (GOS) in the hydrogenic approach [40, 43, 50]. This fact allows to use the Bragg rule [51] for determining the ELF of the inner shells for a compound target as the sum of their atomic constituents [28]:

$$\begin{aligned}\mathrm{Im}\left[\frac{-1}{\varepsilon\,(k,\omega)}\right]_{\mathrm{inner}} &= \mathscr{N}\sum_j \alpha_j \frac{\mathrm{ELF}_j(k,\omega)}{\mathscr{N}_j} \\ &= \frac{2\pi^2\mathscr{N}}{\omega}\sum_j \alpha_j \sum_{n\ell}\frac{\mathrm{d}f^j_{n\ell}(k,\omega)}{\mathrm{d}\omega}\Theta(\omega-\omega^j_{\mathrm{ionis},n\ell}) ,\end{aligned} \tag{12}$$

where $\mathscr{N}$ is the molecular density of the target, α_j, $\mathrm{ELF}_j(k,\omega)$ and $\mathscr{N}_j$ are, respectively, the stoichiometry coefficient, the ELF of the *jth* atom and the atomic density of the *jth* element, $\mathrm{d}f^j_{n\ell}(k,\omega)/\mathrm{d}\omega$ is the hydrogenic GOS corresponding to the (n,ℓ)-

subshell of the jth element, and $\hbar\omega^{j}_{\mathrm{ionis},n\ell}$ is the ionisation energy of the $(n,\,\ell)$-subshell of the jth-element in the compound target. $\Theta(...)$ represents the Heaviside step function.

Due to the complex structure of the ELF for real materials, it is suitable to describe the outer-shells contribution to the ELF, $\mathrm{Im}\left[-1/\varepsilon\,(k,\,\omega)\right]_{\mathrm{outer}}$, by a linear combination of Mermin-type ELF (MELF), which must be fitted to the experimental optical ELF ($k = 0$), namely,

$$\mathrm{Im}\left[\frac{-1}{\varepsilon\,(k=0,\,\omega)}\right]_{\mathrm{outer}} = \mathrm{Im}\left[\frac{-1}{\varepsilon\,(k=0,\,\omega)}\right]_{\mathrm{exp}} = \sum_i A_i \mathrm{Im}\left[\frac{-1}{\varepsilon_{\mathrm{M}}\,(k=0,\,\omega;\,\omega_i,\,\gamma_i)}\right]\Theta(\omega-\omega_{\mathrm{th},i})\,, \quad (13)$$

with ε_{M} being the Mermin dielectric function [49], given by:

$$\varepsilon_{\mathrm{M}}(k,\,\omega) = 1 + \frac{(1+i\gamma/\omega)\left[\varepsilon_{\mathrm{L}}(k,\,\omega+i\gamma)-1\right]}{1+(i\gamma/\omega)\left[\varepsilon_{\mathrm{L}}(k,\,\omega+i\gamma)-1\right]/\left[\varepsilon_{\mathrm{L}}(k,\,0)-1\right]}, \quad (14)$$

where ε_{L} is the Lindhard dielectric function [22, 52, 53], which provides an analytic expression for the dielectric response function of a homogeneous free-electron gas, where plasmons are undamped electronic excitations. However, experimental evidence indicates that a strong damping mechanism exists at all k for most materials. To solve this problem, the Mermin dielectric function phenomenologically modifies the Lindhard dielectric function by including plasmon damping through phonon-assisted electronic transitions. It should be noted that at the optical limit the Mermin and the Drude ELF are equivalent.

In Eq. (13) the coefficients A_i account for the intensity of each resonance in the experimental energy loss spectrum (i.e., the intensity of their oscillator strengths), $\hbar\omega_i$ and $\hbar\gamma_i$ represent the position and width of each excitation and $\hbar\omega_{\mathrm{th},i}$ is a threshold energy, usually the band gap energy, below which electronic excitations are not possible.

In summary, the fitting parameters A_i, ω_i and γ_i of the optical ELF in Eq. (13) are chosen in such a way that it reproduces the main features of the experimental optical ELF and fulfils physically motivated restrictions, such as the Kramers-Kronig (KK) sum rule [25]:

$$\frac{2}{\pi}\int_0^\infty \mathrm{d}\omega\,\frac{1}{\omega}\mathrm{Im}\left[\frac{-1}{\varepsilon(k=0,\,\omega)}\right] = 1 - \frac{1}{n^2(0)} \quad (15)$$

and the f-sum rule (or Thomas-Reiche-Kuhn sum rule):

$$Z_2 = \frac{m}{2\pi^2\mathscr{N}e^2}\int_0^\infty \mathrm{d}\omega\,\omega\mathrm{Im}\left[\frac{-1}{\varepsilon(k=0,\,\omega)}\right]. \quad (16)$$

$n(0)$ represents the refractive index at the static limit, whereas Z_2 is the target atomic number (per molecule). The KK sum rule, Eq. (15), guarantees a good behaviour of the ELF at low energy transfers. The f-sum rule, Eq. (16), links the ELF to the number of target electrons per molecule that can be excited by the projectile; it must be fulfilled for a good behaviour of the ELF at intermediate and high energy transfers.

An important advantage of the MELF-GOS model is that the extension from the optical data to $k \neq 0$ is automatically achieved through the analytic properties of the Mermin dielectric function, therefore no extra extension algorithms have to be introduced.

In order to test the accuracy of the MELF-GOS model, we calculate the Bethe surface of liquid water and compare with experimental measurements from inelastic x-ray scattering spectroscopy (IXSS) [54, 55]. Figure 1 shows the experimental data for the ELF of liquid water from $k = 0$ to $k = 3.59$ a.u. (symbols), together with the calculations obtained by the MELF-GOS model (lines). The very good agreement does not happen for other extended optical-data models (see [41]), which means that the inclusion of the damping in the electronic excitations is indispensable. Therefore, by starting from the experimental ELF at the optical limit, the MELF-GOS methodology can realistically predict the excitation spectrum of liquid water (and any other target) over the entire plane of energy and momentum transfers.

The dielectric formalism, together with a realistic description of the electronic properties of the target by the MELF-GOS model, has been successfully applied to calculate electronic energy-loss quantities for ions and electrons in a large number of inorganic and biological materials (elemental and compounds) [23–26, 40, 48, 56–65], which compare satisfactorily well with available experimental data.

As we discussed in Sect. 2, the SEICS code needs as input data the stopping power S_q and the energy-loss straggling Ω_q^2 for each charge state q of the projectiles in the irradiated target. Now we apply this methodology to calculate these quantities for proton beams in liquid water, as it is the main constituent of living tissues.

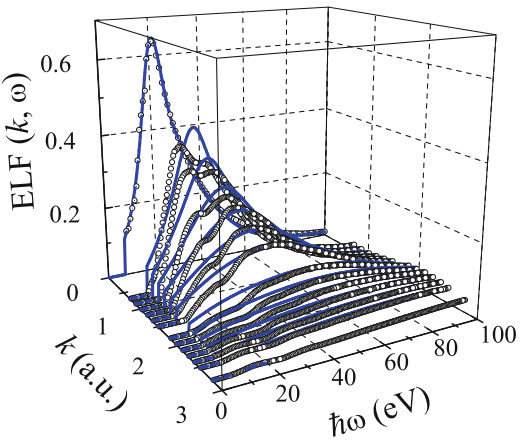

Fig. 1 Energy loss function (ELF) of liquid water as a function of energy $\hbar\omega$ and momentum transfer $\hbar k$. *Symbols* are experimental data from Hayashi [55] and *lines* represent the calculations from the MELF-GOS model

Before comparing the calculated energy-loss quantities with experimental data it is necessary to take into account that due to electron capture and loss processes by the projectile, the ion can be in different charge states q. The probability that the projectile reaches a given (equilibrium) charge state q at a given energy T is $\phi_q(T)$. Therefore, the stopping quantities are evaluated as:

$$S(T) = \sum_{q=0}^{Z_1} \phi_q(T)\, S_q(T)\ , \qquad \Omega^2(T) = \sum_{q=0}^{Z_1} \phi_q(T)\, \Omega_q^2(T)\ . \tag{17}$$

The equilibrium charge fractions $\phi_q(T)$ of the projectile, which depend on its energy and the target nature, are taken from a parameterisation to experimental data [66]. In Fig. 2 we show by solid lines the calculated stopping power S and energy-loss straggling Ω^2 for proton beams in liquid water as a function of the incident energy. S is compared with available experimental data (symbols) for liquid water [29, 30, 67] and ice [68–70]. The semiempirical results provided by the SRIM code [14] are depict by a grey dashed line, whereas the grey dash-dotted line corresponds to the stopping power collected in the ICRU Report 49 [71]. The predictions at high energies of all the models agree (among them and) with the newest experimental data in liquid water [67]. However, at energies aroud and lower than the stopping power maximum, the predictions of the models clearly disagree among them and depart from the available experimental data (although these are not for liquid water but for ice). Both SRIM and ICRU curves show a good agreement with the experimental data for ice, because they use a parameterisation to these available experimental data. We note that at low proton energies the inclusion of the electron charge-exchange

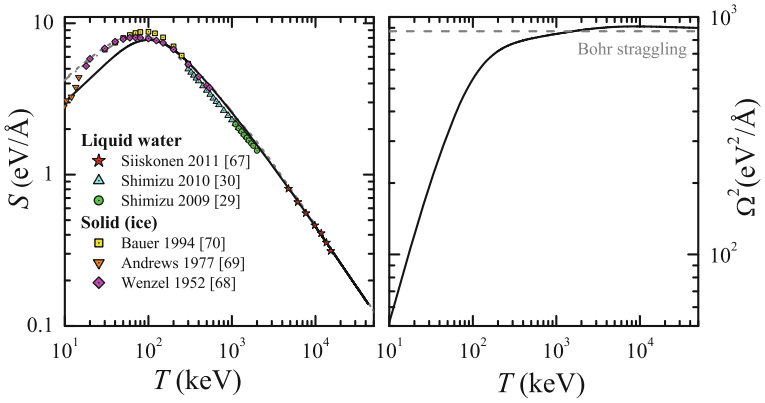

Fig. 2 **a** Stopping power of liquid water for an incident proton beam as a function of its energy. *Symbols* are experimental data for liquid water and ice. *Solid line* corresponds to calculations from the MELF-GOS model. Results from semi-empirical models, such as SRIM [14] (*grey dashed line*) and ICRU [71] (*grey dash-dotted line*), are also depicted. **b** Energy-loss straggling for protons in liquid water

process is essential to obtain suitable stopping power data. For a detailed discussion of the influence of several theoretical models in the stopping power calculations, the interested reader can consult Refs. [28, 41]. It is also interesting to note the differences between the experimental data for protons in liquid water at intermediate energies [29, 30] and the theoretical results. These experimental data rely on the measurement of the energy distributions of proton beams after traversing a liquid water jet, and on the interpretation of these energy distributions by Monte Carlo simulation. In Sect. 3 we will show that the stopping power at intermediate energy obtained in Refs. [29, 30] is questionable.

Moreover, at high projectile energies the SEICS code uses the Bethe stopping power (see Eq. (5)), where the mean excitation energy I of the material must be known, which only depends on the electronic structure of the target, and is defined in terms of the target ELF by the relation:

$$\ln I = \frac{\int_0^\infty \mathrm{d}\omega \, \ln(\omega) \, \omega \mathrm{Im}[-1/\varepsilon(0,\omega)]}{\int_0^\infty \mathrm{d}\omega \, \omega \mathrm{Im}[-1/\varepsilon(0,\omega)]} \, . \tag{18}$$

Therefore, accurate values of I are desirable, in particular for biological materials, where a few percent in the uncertainty of the I values might cause sizeable changes in the range and stopping maximum (i.e., the Bragg peak) of therapeutic ion beams, which have energies of the order of several hundreds of MeV/u. With the MELF-GOS model a value of the mean excitation energy 79.4 eV for liquid water is obtained. A comparison between different I values calculated from several models and several biological targets can be found in Ref. [28].

2.2 Elastic Collisions

The simulation code SEICS also considers multiple elastic scattering among the target nuclei and the projectile. These very frequent events modify the trajectory of the projectile providing its angular deflection (i.e., lateral spreading) and contribute to the energy-loss at low energies at the end of its travel, especially at the distal part of the Bragg peak, which affects the range of the projectile.

The elastic collisions are implemented in the code through a Monte Carlo algorithm [72, 73] that provides the projectile scattering angle and the corresponding elastic energy loss at each collision. The path length L_{el} of the projectile between two successive collisions with the target atoms is given by:

$$L_{\mathrm{el}} = -\frac{\ln \xi_3}{\sum_i \Lambda_{\mathrm{el},i}} \, , \tag{19}$$

where $\Lambda_{\mathrm{el},i}$ is the projectile inverse mean free path for having an elastic interaction with the i-atom of the target compound. Therefore $\sum_i \Lambda_{\mathrm{el},i}$ is the total macroscopic

cross section for having an elastic collision with the target nuclei. We assume that each target atom is an effective scattering centre having a spherical volume with radius $r_0 = 1/(2\mathscr{N}^{1/3})$, where $\mathscr{N}$ is the target molecular density. To determine the type of the target atom that undergoes the collision with the projectile, we suppose that the collision probability with the i-atom type is proportional to the fractional contribution made by each atom to the total cross section [74]. The scattering between the projectile and the target atom is described by a screened Coulomb potential; here we use the universal interatomic potential [14] with the universal screening length. Therefore, the polar and the azimuthal scattering angles can be determined as well as the energy loss in the scattering process.

Summarising, the projectile direction of motion before the n-collision is defined by the polar angle Θ_{n-1} and the azimuthal angle Ψ_{n-1} in the laboratory frame of reference. The path length $L_{\rm el}$ until the next elastic collision is determined by using Eq. (19); after an elapsed time $L_{\rm el}/v$, the n-collision takes place and we determine the i-type of target atom that is involved in the collision. Then, the scattering angles (polar and azimuthal), with respect to the direction of motion, are calculated and a new direction of motion, as well the modulus of the projectile velocity, in the laboratory frame of reference is obtained after the n-collision [73]. Once the velocity (modulus and direction) is known after the n-collision, the next collision takes place following the same steps that have been explained in the preceding paragraphs. A detailed description of the expressions used for the elastic scattering is presented in Ref. [35].

2.3 Charge Exchange Processes: Electron Capture and Loss

The capture and loss of electrons by the projectile, when it moves through the target, is included in the simulation code by a Monte Carlo procedure [34]. This affects the stopping force since it depends on the charge-state of the projectile.

The path length $L_{\rm C\&L}$ of the projectile between two successive electronic capture or loss events is given by:

$$L_{\rm C\&L} = -\frac{\ln \xi_7}{\Lambda_{\rm C} + \Lambda_{\rm L}} \,, \tag{20}$$

where $\Lambda_{\rm C}$ and $\Lambda_{\rm L}$ are the inverse mean free paths for electron capture and electron loss, respectively, both depending on the charge-state q of the projectile. We assume that the electron-loss cross section is proportional to both the geometrical cross section of the projectile and the number of its bound electrons. The inverse mean free path for electron capture, if multiple-electron processes are neglected, can be obtained from the equilibrium relation:

$$\Lambda_{\rm C}(q+1 \to q) = \frac{\phi_q}{\phi_{q+1}} \, \Lambda_{\rm L}(q \to q+1) \,, \tag{21}$$

where ϕ_q and ϕ_{q+1} are the equilibrium fractions of the q and $q+1$ charge-states, respectively. For hydrogen projectiles:

$$\phi_0 + \phi_{+1} = 1 \,, \tag{22}$$

$$\phi_{+1} = \langle q \rangle \,, \tag{23}$$

where $\langle q \rangle$ is the average charge-state obtained through a fit to experimental data [66]. Since the probabilities of electron loss or electron capture by a projectile with charge-state q are proportional to the corresponding inverse mean free paths, it is possible to determine the new projectile charge-state from Eq. (23). In summary, according to this model we obtain the path length $L_{\mathrm{C\&L}}$ using Eq. (20); after an elapsed time $L_{\mathrm{C\&L}}/v$, either an electronic capture or loss event takes place determined according to their respective probabilities (see Ref. [35] for more details). We also take into account that electron capture and loss processes contribute to the energy loss of the projectile in an amount that is calculated according to the theoretical models outlined in Refs. [48, 75].

2.4 Nuclear Fragmentation Reactions

An accurate simulation of the propagation and energy deposition of swift protons in biological media at energies typically used in hadron therapy (several hundred of MeV) requires the inclusion of nuclear fragmentation reactions between primary protons and target nuclei. Complex processes occur in these collisions, which imply the excitation of the target nucleus, its fragmentation, the emission of secondary energetic particles (such as neutrons, photons, secondary protons or heavier particles), and the relaxation of the residual nucleus.

Nuclear fragmentation processes are included in the SEICS code assuming some pertinent simplifications. We consider that primary protons are removed from the beam according to their total non-elastic nuclear cross section, with a fraction of their residual energy being locally deposited.

According to the standard Monte Carlo procedure, the distance L_{frag} between two consecutive nuclear fragmentation collisions can be calculated as:

$$L_{\mathrm{frag}}(T) = -\lambda_{\mathrm{frag}}(T) \ln \xi_9 \,, \tag{24}$$

where λ_{frag} is the fragmentation mean free path given by:

$$\lambda_{\mathrm{frag}}(T) = \frac{A_2}{N_{\mathrm{A}}\, \rho\, \sigma_{\mathrm{frag}}(T)} \,, \tag{25}$$

with A_2 and ρ being, respectively, the total mass number (sum of the elemental constituents mass numbers) and the density of the compound target. N_{A} is the Avogadro

number. σ_{frag} is the microscopic nuclear reaction cross section for the compound, i.e., the sum of the cross sections $\sigma_{\text{frag},i}$ of its constituents weighted by the corresponding stoichiometric content α_i of each element:

$$\sigma_{\text{frag}} = \sum_i \alpha_i \sigma_{\text{frag},i} \ ; \tag{26}$$

the values of $\sigma_{\text{frag},i}$ are chosen from recommended inelastic cross-sections compilations [76]. The fragmentation mean free path for protons in liquid water is shown in Fig. 3a as a function of the proton energy.

However, Eq. (24) is only valid when the mean free path does not change too much along the collision path. Since the change in the energy of the projectiles is large, due to the large values of the mean free path, we use an alternative algorithm to determine the distance at which the nuclear fragmentation reaction takes place. The formula for the exponential loss of particles in the beam is:

$$N(s + \mathrm{d}s) = N(s)\, \mathrm{e}^{-\mathrm{d}s/\lambda_{\text{frag}}} \ , \tag{27}$$

where $N(s)$ is the number of remaining particles at a distance s, with ds being a differential path; $1 - N(s + \mathrm{d}s)/N(s)$ is a quantity between 0 and 1, which can be interpreted as the probability for a nuclear fragmentation to occur in this differential path ds. A random number is sampled in each differential path and, if its value is less or equal than $1 - N(s + \mathrm{d}s)/N(s)$, then the primary proton disappears and deposits locally part of its energy. We consider that the energy transferred to neutral ejectiles (neutrons and gamma particles) escapes out of the treatment region and is lost [77], whereas the energy imparted to charged secondaries (protons, deuterons, tritons, alpha particles...) is deposited locally. Figure 3b shows the energy fraction f_{ejectile} transferred to different ejectiles, as recommended by the ICRU Report 63 [76].

3 Benchmarking the SEICS Code and the Experimental Stopping Power of Protons in Liquid Water

In this section we will benchmark the SEICS code (and one of its main ingredients, namely our calculated stopping power of liquid water) by comparing the simulated energy distribution of protons directed to a liquid water jet with the corresponding experimental data reported in Ref. [30].

One of the most relevant inputs for the simulation of the interaction of charged particles with condensed matter is the stopping power. Therefore an accurate determination of the stopping power of energetic protons in liquid water, as a subrogate of living tissues, is essential in hadron therapy [78, 79]. However only two sets of experimental data exist, due to the Kyoto group [30] and the Jyväskylä group [67]. Both are depicted in Fig. 2, together with theoretical curves as well as experimental stopping power of ice. Our calculated stopping power from the dielectric formalism

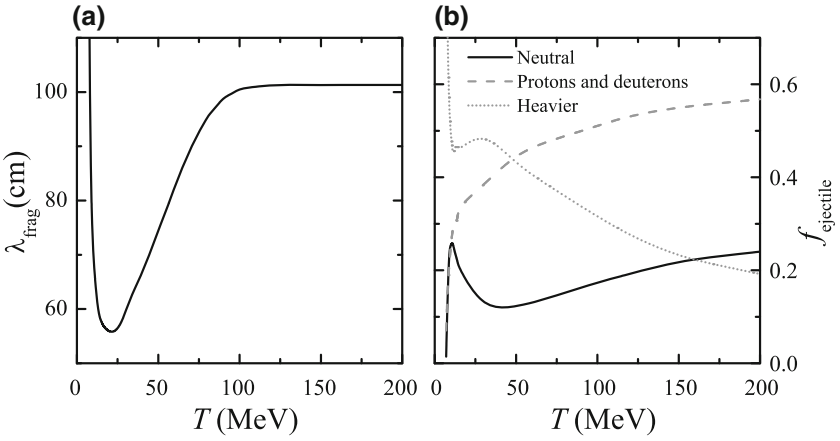

Fig. 3 **a** Nuclear fragmentation mean free path for protons in liquid water as a function of the incident energy, Eq. (25). **b** Fraction $f_{ejectile}$ of residual energy transferred from the incident proton to different ejectiles (neutral, protons and deuterons, and heavier particles) in liquid water, according to ICRU Report 63 data [76], as a function of the incident proton energy T

and the MELF-GOS model agrees very well with the data obtained by Siiskonen et al. [67]. However it is larger than the experimental data provided by Shimizu et al. [30]. This discrepancy can be understood from the way in which the experimental stopping powers were obtained by each group. Whereas the former [67] were derived directly from transmission measurements in a thin liquid water foil, the latter [30] was indirectly obtained though a fitting procedure from the energy spectrum at different exit angles of a proton beam after crossing a super-thin water jet.

The experimental stopping power data reported by the Kyoto group [29] were obtained by using the stopping power and the jet diameter as fitting parameters in the simulations performed with the GEANT4 code [16], until reaching satisfactory agreement with the experimental energy spectra. Figure 4 shows by symbols the experimental energy distributions for 2 MeV protons in liquid water at 10, 30 and 50 mrad; the GEANT4 simulations are depicted by dotted lines. In this figure, the energy of the ions after leaving the target, and when they reach the detector, is denoted by E.

However, these proton energy distributions after interaction with the liquid water jet can be satisfactorily reproduced using the SEICS code using the jet diameter as the only fitting parameter. We only need to take a 48.25 μm jet diameter (i.e., 3.5 % reduction compared to its nominal value) to obtain a very good agreement with the experimental distributions, being ever better than the comparison of GEANT4.

Proceeding in this manner we have validated the performance of the SEICS code for a suitable simulation of the motion and energy deposition of protons through a condensed target, and also, the reliability of our calculated stopping power values (solid curve in Fig. 2), which was obtained from the dielectric formalism and the MELF-GOS methodology. These results endorse what could be expected from the good agreement of our model-ELF for liquid water at several momentum transfers,

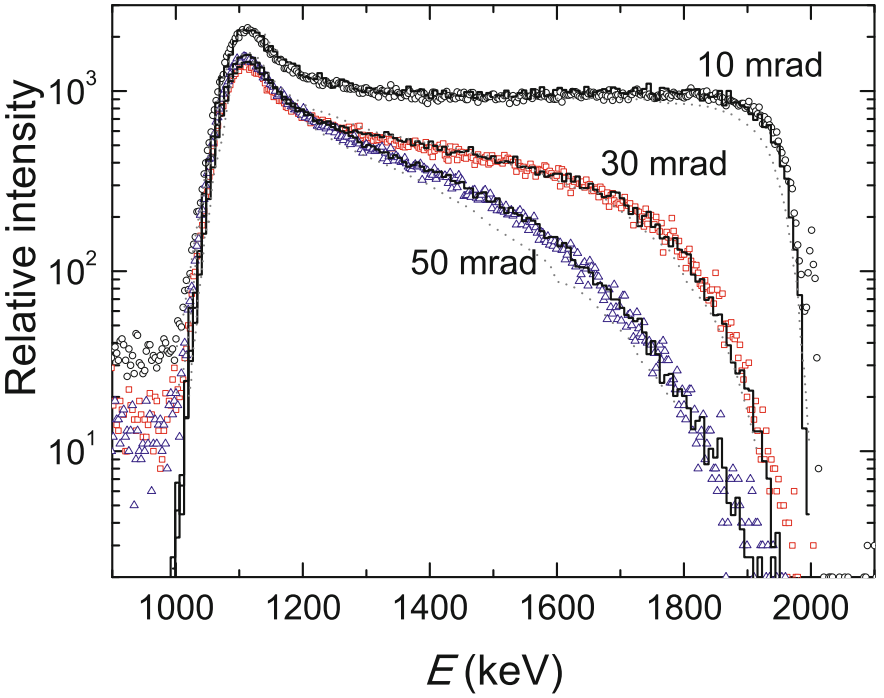

Fig. 4 Proton energy distributions at 10, 30 and 50 mrad after a 2 MeV proton beam interacts with a liquid water jet. *Symbols* correspond to experimental measurements [30]. *Dotted lines* are the distributions obtained with GEANT4, where the jet diameter and the liquid water stopping power had to be used as fitting parameters. *Solid lines* represent the results obtained with the SEICS code, where only the jet diameter was used as a fitting parameter, whereas the stopping power was the one provided by the dielectric formalism and the MELF-GOS methodology

which did agree very well with experimental measurements (Fig. 1), as well as the mean excitation energy $I = 79.4$ eV for liquid water predicted by the MELF-GOS method (see Eq. (18)), which is within the recent recommendation of 79.2 ± 1.6 eV given in Ref. [79].

4 Evaluation of Useful Quantities for Ion Beam Cancer Therapy

We will apply the simulation code SEICS to evaluate several quantities that are relevant in ion beam cancer therapy. We will focus our attention in the interaction of proton beams with liquid water, which is the main constituent of biological systems, and one of the most studied targets both theoretically and experimentally. The energy

of the proton beam will be of the order of several hundred of MeV, as it is currently used in hadron therapy.

We will obtain the distribution of the dose deposited in the target as a function the depth (the Bragg curve), evaluating the influence of the different processes included in the code to describe the propagation of the projectiles through the target. The depth-dose curves will be compared to available experimental data.

From the detailed simulation it is also possible to extract the lateral dose distribution of the proton beams in the target, which is mainly due to elastic collisions. This can be quantified through the root mean square radius of the beam, which is parameterised as a function of the depth and energy of the incident projectiles.

Also, the energy distributions of the proton beam as a function of the depth in the target will be simulated, due to its significance in the generation of secondary electrons in the Bragg peak due to the proton impact.

4.1 Depth-Dose Distribution of Protons in Liquid Water

The precise knowledge of the energy deposited in the target by a proton beam as a function of the depth in the target (the depth-dose curve) is essential in proton therapy. This will allow a better control of the position of the Bragg peak, and of the energy deposited in it, as well as the energy deposited in the entrance-plateau region and distal part, where minimum damage is desired.

Due to its structure, the simulation code can be used to identify the role that each interaction process (elastic scattering, stopping power, energy-loss straggling, electron capture and loss, nuclear fragmentation reactions) has in its shape, since each process can be switched on and off in the simulations. Figure 5 represents the depth-dose profile of a 150 MeV proton beam in liquid water obtained with the SEICS code by removing in a controlled manner the contribution of different phenomena to the final result. The complete simulation, where all the processes (described in Sect. 2) are included is depicted by a solid line. Different processes have been eliminated from the simulation to analyse their contribution to the full simulation. Removing the energy-loss straggling (dotted line) has a big effect in the depth-dose curve, producing the appearance of an (unphysical) very sharp Bragg peak. Ignoring multiple elastic scattering (not shown in the figure) has a negligible influence on the depth-dose curve. Finally, a simulation without nuclear fragmentation reactions (dashed line) results in a broader (and slightly higher) peak and also in a reduction of energy deposited at the entrance region. Further information can be found for smaller proton incident energies in Refs. [21, 35, 80]. The choice of the stopping power used as input in the SEICS code (not shown in Fig. 5) mainly affects the range of the protons in the medium [41], and therefore the position of the Bragg peak [5, 78, 79, 81]. In all our calculations we use the electronic energy loss derived from the dielectric formalism and the MELF-GOS methodology, as described in Sect. 2.1.

The inclusion of the nuclear fragmentation reactions is an essential ingredient for projectiles having the typical energies used in hadron therapy, which is of the

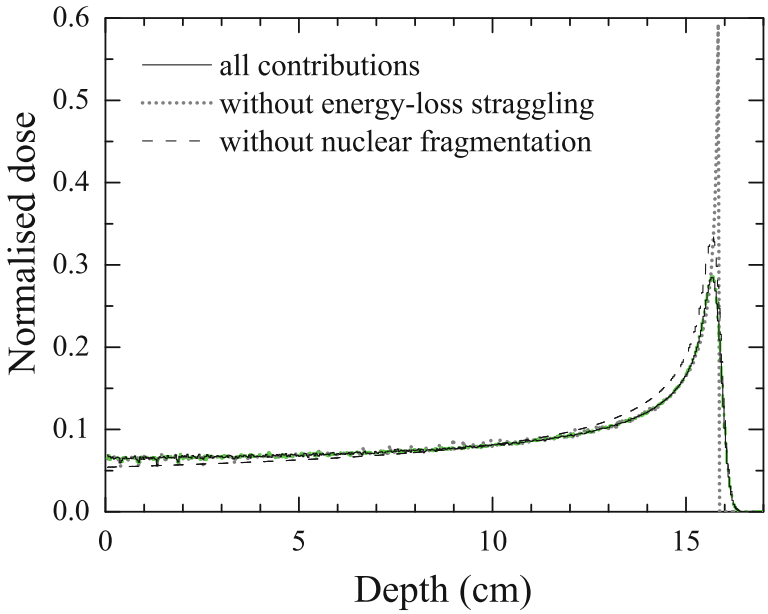

Fig. 5 Depth-dose distribution of a 150 MeV proton beam in liquid water simulated by the SEICS code (*solid line*). The relative contribution of different processes to the final result is considered by removing them from the simulation: without energy-loss straggling (*dotted line*), and without nuclear fragmentation (*dashed line*)

order of a few hundreds of MeV/u. We check our approach to implement the nuclear fragmentation reactions in the SEICS code comparing our results for depth-dose curves with available experimental data.

Figure 6 compares with experimental measurements [82] our simulated depth-dose curve for a 221.8 MeV proton beam in liquid water. Both curves are normalised to unit area. As it can be seen, the SEICS results, including the complete description of nuclear fragmentation reactions, perfectly agrees with the experiments at practically all the depths, except at the entrance of the target, where the simulation slightly overestimates the dose, as expected. In this figure we can also see the influence of the nuclear reaction model in the results. The dotted curve shows the simulated results when the nuclear fragmentation reactions are switched off. Clearly, it can not reproduce the experimental data. The dashed curve shows the results with nuclear reactions, but only removing the primary protons, without accounting for secondary particles, as it is done in some simpler approaches [83], which slightly improves the results without nuclear reactions. But the effect of secondary particles has to be taken into account, at least in an approximate manner as we have done, to obtain results in accordance with experimental data.

The good performance of our code can be further checked by comparing in Fig. 7 the simulated depth-dose curves with available experimental data for protons in

liquid water at several energies. In all cases, there is an excellent agreement with the experimental data [82] for all the energies analysed.

It is noteworthy that the simple model we have used for nuclear fragmentation reactions allows a very nice comparison with experiments, without the necessity of implementing complex nuclear models.

4.2 Lateral Spreading of the Depth-Dose Distribution

Besides predicting with enough accuracy the depth-dose curves, in order to achieve high precision in hadron therapy treatment planning, another fundamental requisite is to know the lateral spreading of the beam with respect to the incident direction.

Multiple elastic scattering is the main responsible of the transversal deviations of the projectile trajectory, which results in the lateral spreading of the proton dose distribution, with the subsequent loss of precision in oncological treatment planning.

In what follows, we use the SEICS code to map the energy deposited in the target by the projectiles, both in the longitudinal and transverse directions of the incident beam.

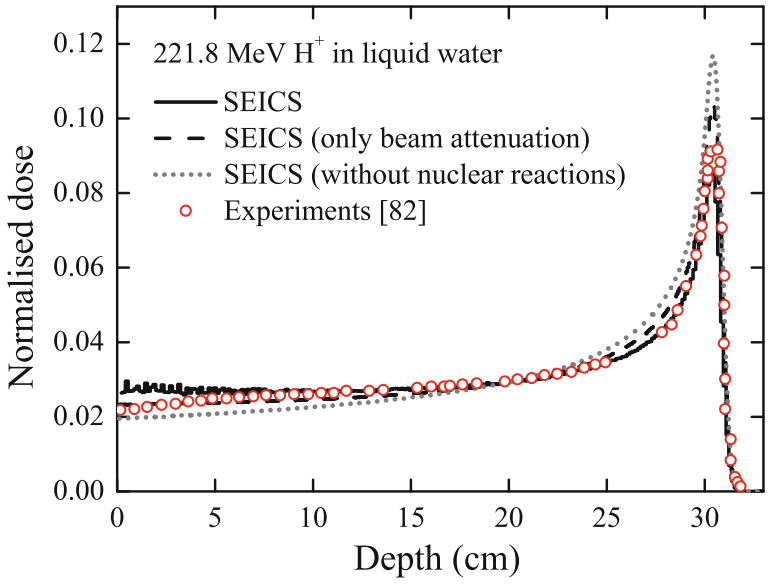

Fig. 6 Depth dose distribution in liquid water of a 221.8 MeV proton beam; experimental data are represented by *symbols* [82], whereas the *solid line* represents the results provided by the SEICS code. Simulations without nuclear reactions are depicted by a *dotted line* and with nuclear reactions but without including local energy deposition are shown by a *dashed line*. All the depth dose distributions are normalised to have unit area

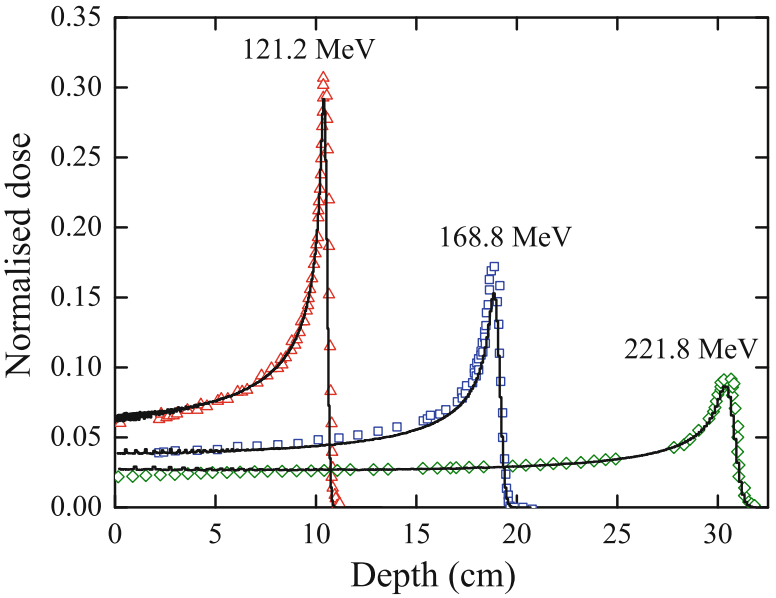

Fig. 7 Depth-dose curves of proton beams incident with different energies on liquid water. *Symbols* represent experimental data [82], whereas *solid lines* are the simulations obtained with the SEICS code. The depth-dose distributions are normalised to have unit area

We consider an initially monoenergetic proton pencil beam directed along the z-axis at therapeutic energies travelling in liquid water. A degradation of the proton energy occurs due mainly as a consequence of inelastic collisions, and a broadening of the beam takes place due to the multiple elastic scattering. The three-dimensional distribution of deposited energy along the projectile track can be described through the lateral dose distribution $\Phi(z, r)$, i.e., the dose delivered in the target at each depth z and at a given radial distance r perpendicular to the projectile incident direction. Due to the azimuthal symmetry of the problem, the x and y directions are equivalent, therefore in order to visualize the lateral dispersion of the dose we use the function $\Phi(z, x) = \Phi(z)N(z, x)/N(z)$, where $\Phi(z)$ is the total dose at a given depth z, that is, the depth-dose curve. $N(z, x)$ represents the number of particles at a given depth z and at a given lateral distance x, with $N(z)$ being the total number of projectiles at a depth z. Note that $N(z)$ is not constant, since the number of projectiles in the beam decreases with the depth due to the stopping of particles and the nuclear fragmentation processes.

In Fig. 8 we represent the simulated lateral distribution of the deposited dose for a 150 MeV proton beam in liquid water obtained with the SEICS code. It has to be noted the difference in the longitudinal and lateral scales, being the latter less than 10 % of the former, demonstrating the small lateral deflection of proton beams, which is one of their interesting features for treatment purposes. The larger concentration of deposited energy takes place along the beam entrance axis. However, due to multiple

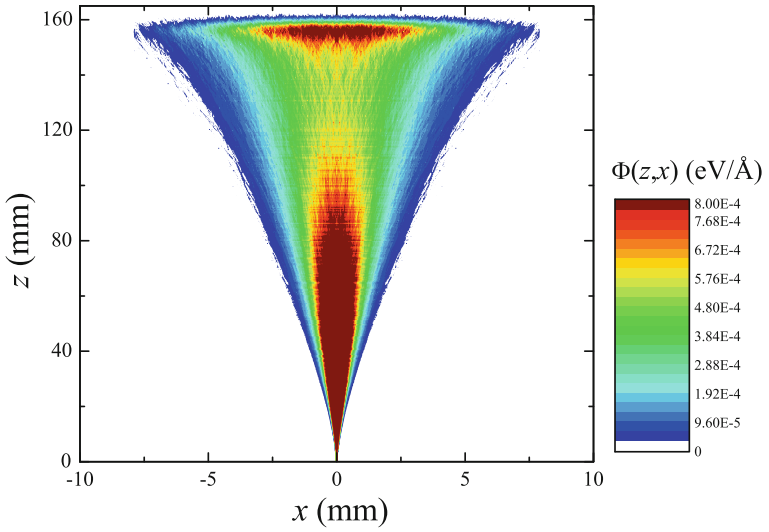

Fig. 8 Simulated lateral distribution of the dose deposited in liquid water by a 150 MeV proton beam, as a function of the depth z and the lateral distance x from the initial beam direction

elastic scattering there is a lateral spreading of the energy deposited that grows as the depth increases and reaches its maximum value around the Bragg peak. Because of this spread, the lateral dose presents two maxima along the initial projectile direction (i.e., the z axis), one at the Bragg peak depth, where the depth-dose curve is maximum, and another one at the very beginning of the protons track, where all the particles are concentrated in a small region because practically no elastic scattering has occurred yet. Although the total dose is smaller at the entrance plateau as compared to the Bragg peak region, the concentration of all the particles in small radial distances gives place to this maximum. Nonetheless, the integration of the lateral dose distribution recovers the expected shape of the integral depth-dose curve.

The lateral profile of the dose deposition pattern depends on the radial distribution of particles along the beam path, which can be represented by its root mean square radius $r_{\mathrm{rms}} = \langle r^2 \rangle^{1/2} = \sqrt{\langle x^2 \rangle + \langle y^2 \rangle}$, which is a function of the depth z. As the SEICS code follows the trajectories of the protons through the target, it is possible to evaluate r_{rms} at each depth, which indicates how much the incident particles scatter along their path. It has been shown [84] that our simulated results for r_{rms} of a proton pencil beam in liquid water agree with experimental data [85] as well as with an analytical model [86]. Although r_{rms} depends on the path traversed in the medium, on the atomic weight of the target and on the charge and energy of the incident projectiles, our simulations indicate that the quotient between the r_{rms} for a proton beam at the Bragg peak depth, $(r_{\mathrm{rms}})_{\mathrm{max}}$, and the Bragg peak depth, z_{max}, is always around 3 %, that is $(r_{\mathrm{rms}})_{\mathrm{max}} \sim 0.03 z_{\mathrm{max}}$, independently of the initial proton energy in the range from 5 to 250 MeV for liquid water. For a 100 MeV proton beam, typically

used in hadron therapy, the spread of the beam in liquid water at the Bragg peak is around 2 mm, whereas at 200 MeV it increases up to around 7 mm.

In the same proton energy range (5–250 MeV), our simulations predict that r_{rms} increases with the depth z following a parabolic dependence and suddenly falls down at the distal part of the Bragg peak, since only a few projectiles travel in almost straight line to reach these deeper regions, whereas most of them, which undergo multiple elastic collisions, deviate from their initial direction and stop at lower depths. As the simulation of the lateral dose distribution for each proton energy is very time consuming, it is convenient to have an analytical expression that approximately provides the lateral spreading of the beam as a function of the depth. This is accomplished through the following parabolic dependence of r_{rms} with the depth z:

$$r_{\mathrm{rms}}(\mu\mathrm{m}) = C_1\, z(\mu\mathrm{m}) + C_2(\mu\mathrm{m}^{-1})\, z^2(\mu\mathrm{m}^2)\ . \tag{28}$$

The parameters C_1 and C_2 depend on the projectile initial energy, and can be found by the best fit to the simulated r_{rms}-curves for several initial proton beam energies T_0. These parameters are shown in Fig. 9 by symbols. It is found that both parameters follow a logarithmic behaviour with the initial proton energy T_0:

$$C_i = b_i\,[T_0(\mathrm{MeV})]^{a_i}\ , \tag{29}$$

where the constants a_i and b_i (the subscript i being associated to each C_i) are determined by the best fit to the C_i of the previous equation, shown by solid lines in Fig. 9. For protons in liquid water, these constants have the following values: $a_1 = -0.058$, $a_2 = -1.87$, $b_1 = 9.39 \times 10^{-3}$ and $b_2 = 1.56 \times 10^{-3}$.

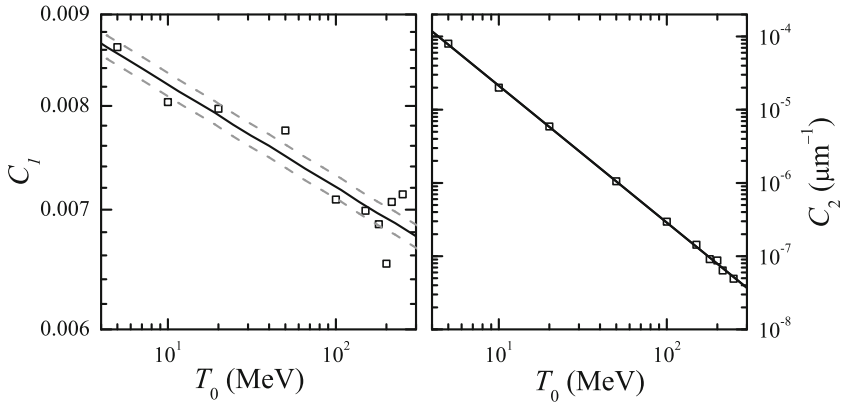

Fig. 9 Parameters C_1 and C_2 used to fit the r_{rms} of a proton pencil beam in liquid water to a parabola as a function of the initial proton energy. *Symbols* represent the results obtained with the SEICS code, *solid lines* are the least squares fits to these results and *dashed lines* represent their absolute error. In the case of C_2 the *lines* delimiting the error are indistinguishable from the *solid line*

As the lateral spread of the proton dose distribution due to multiple elastic scattering is one of the main causes of the spatial degradation of the Bragg peak, with the subsequent loss of precision required for a successful oncological treatment, a careful characterisation of the lateral spread of the dose deposited in a target of biological interest is of importance for improving the accuracy of clinical treatment planning in hadron therapy. The parameterisation we have obtained for r_{rms} as a function of the penetration depth z and the initial proton energy T_0 allows a quick calculation of r_{rms} for any proton energy and depth in liquid water.

4.3 Energy Distribution of the Proton Beam Along the Bragg Curve

Due to the stochastic nature of the interactions that take place between the projectile and the irradiated target, a monoenergetic distribution of the incident beam turns into an energy distribution as the particles of the beam move through the target. This distribution depends on the target nature, on the initial energy of the beam, and on the path travelled through the target. A detailed knowledge of the projectile energy distributions is very important since the generation of secondary electrons in the target due to proton impact strongly depends on the projectile energy. In this section we will study, by the simulation code SEICS, the energy distribution of a proton beam in liquid water and its evolution along the Bragg curve.

The SEICS code enables the calculation of the projectile energy distribution $\mathrm{d}N(T_0, z, T)/\mathrm{d}T$ at any depth z in the target of an initially T_0-monoenergetic proton beam, taking into account the interaction processes described previously (Sects. 2.1, 2.2, 2.3, and 2.4). The energy evolution of a proton beam incident with $T_0 = 150$ MeV in liquid water is shown in Fig. 10, where the mean energy of the beam (grey line) is depicted as a function of the depth, as well as the energy distribution of the proton beam (black lines) at several depths along the Bragg curve. To relate the Bragg peak with the proton beam energy distribution the depth-dose profile is also shown (dashed line). It can be seen how, while the mean energy of the beam decreases, the energy distribution has a Gaussian shape centred at the average energy, which broadens as the depth increases. At the Bragg peak depth, the distribution is centred around 15 MeV, and its full width at half maximum is practically 15 MeV wide.

In general, the proton energy distribution is rather broad around the Bragg peak, especially at its distal part, having a mean value and a full width at half maximum that always are $\sim$10 %T_0, irrespectively of T_0, as we have found from several simulations. The physical origin of the broadening of the energy distribution is elucidated by switching on and off in the simulation code the different interaction phenomena. We find that the widening of the energy distribution is mainly due to the stochastic nature of the electronic interactions, accounted for through the electronic energy-loss straggling, while the multiple elastic scattering has an effect much less noticeable [21].

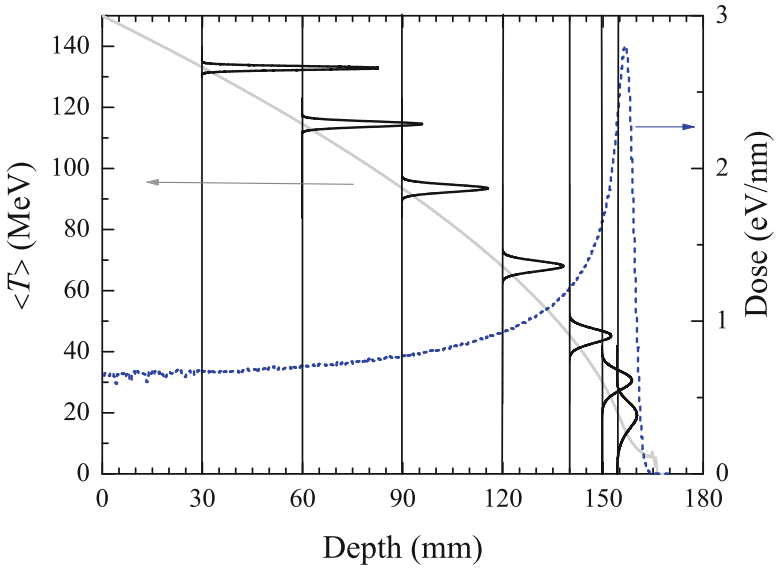

Fig. 10 (*Left axis*) Average energy $\langle T \rangle$ (*grey line*) of protons incident with 150 MeV in liquid water, as a function of the depth. The beam energy distribution at each depth is depicted by *black lines*. (*Right axis*) For comparison purposes, the depth-dose distribution is shown by a *dashed line*

We present in Fig. 11 the simulated energy distribution for a monoenergetic proton beam incident with $T_0 = 150$ MeV in liquid water at three depths around the Bragg peak: z_{80^-} is the depth corresponding to 80 % of the maximum dose before the Bragg peak, $z_{\max}$ is the depth where the maximum dose occurs (which corresponds to the Bragg peak), and z_{80^+} is the depth corresponding to 80 % of the maximum dose after the Bragg peak. The energy distributions are normalised to one incident projectile. It should be noted that when the beam moves through the target there is a reduction in the number of its projectiles due to nuclear reactions and to the energy loss. As it can be clearly seen in the Fig. 11, the proton energy spectrum in the region around the Bragg peak is very broad, especially at its distal part. We also found that the distributions are peacked at lower energies as the depth in the target increases.

4.4 Generation of Secondary Electrons in Biomaterials

Secondary electrons produced by ion impact play a central role in the multiscale picture of ion beam cancer therapy [87], since these electrons transport the energy lost by the projectile around its track at nanometre distances, giving place to a very sharp and intense radial dose distribution. This fact explains the increased radiobiological efficiency of ions compared to photons, for which the microscopic patterns of dose deposition are much more homogeneous [88, 89]. The secondary electrons generated

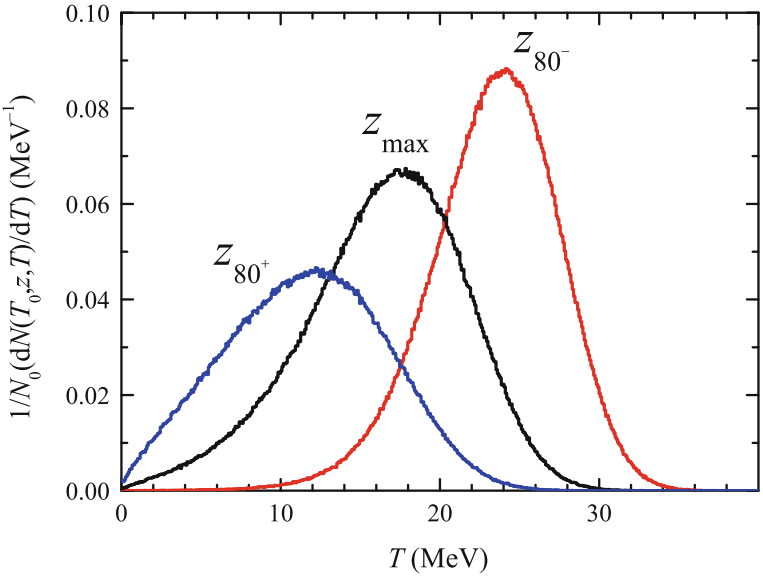

Fig. 11 Energy distributions of protons $\mathrm{d}N(T_0, z, T)/\mathrm{d}T$ for a monoenergetic beam incident with $T_0 = 150$ MeV on liquid water, at depths z_{80^-}, $z_{\max}$ and z_{80^+}, corresponding respectively to 80 % of the maximum dose before the Bragg peak, to the Bragg peak (maximum dose) and to 80 % of the maximum dose at the distal part of the Bragg peak. N_0 is the initial number of incident projectiles. The energy distributions are normalised to one incident projectile

along the proton track can also produce further ionisations, initiating an avalanche effect, leading to the energy transfer to sensitive biomolecular targets, such as DNA, lipids or proteins. Not only the number of emitted electrons is relevant, but also their energy spectrum, since although high energy electrons are capable of producing further ionisations, it has been shown that low energy electrons (below ionisation threshold) can also produce damage to biomolecules by dissociative electron attachment [31, 90].

There are several methodologies to find the energy distributions of secondary electrons generated by ion impact, going from very simple semiclassical models, such as the Rudd formula [91] or the Binary Encounter Approximation (BEA) [92], to complex and sophisticated time-consuming ab initio methods [93]. However, one of the limitations of these models is that they can only be applied with accuracy to some restricted ranges of energies, and specific projectile-target combinations. Therefore, it will be desirable to count on with a universal model applicable to a wide range of energies, any projectile-target system, and also to be simple, in order to be easily implemented in radiobiological models consuming a reasonable computing time.

This section is devoted to present a semiempirical model to calculate the energy distribution of secondary electrons generated by the impact of energetic proton beams in complex condensed biomaterials [94, 95].

A first idea could be using the dielectric formalism, since it provides an adequate framework to describe inelastic interactions of swift projectiles in condensed media. However in this formalism the target electronic response to external perturbations is embodied in the ELF, including electronic excitations and ionisations, which, although being very useful to calculate energy loss quantities (such as the stopping power or the energy-loss straggling, as it was presented in previous sections), complicates the separation of the ionisation information from the excitation one. Only for liquid water, the ELF has been separated in excitation and ionisation contributions, making use of the energies of each shell [96, 97]. This procedure is satisfactory for water, where there are only four outer molecular orbitals, but its generalisation for large and complex macromolecules is not a trivial task.

In what follows, we introduce an extension of the dielectric formalism to describe only the ionisation processes, by some simple but effective approximations, which have been tested against experimental data and other theoretical approaches. It is known that for liquid water excitation processes are practically confined at low transferred energies, while at high energies only ionisations remain [96, 97]. Therefore, it seems appropriate to estimate a mean binding energy, $\overline{B}$, from the ionisation thresholds of all the outer electronic shells, and assume that ionisations or excitations will only occur at energies above or below this threshold, respectively. This semiempirical method allows the calculation of ionisation cross sections for arbitrary biological materials within the dielectric formalism [94, 98].

Let us consider an energetic ion of mass M_1, atomic number Z_1 and charge q, moving with kinetic energy T in a medium characterised by its dielectric function $\varepsilon(k, \omega)$. Assuming that the outer shell electrons of the target can be characterised by a mean binding energy $\overline{B}$, then a secondary electron will be ejected with a kinetic energy $W = \hbar\omega - \overline{B}$. For each (n, ℓ)-subshell of each jth element, characterised by the ionisation energy $B^j_{\text{ionis},n\ell}$, the secondary electrons will be ejected with energy $W = \hbar\omega - B^j_{\text{ionis},n\ell}$. Then, the dielectric framework gives the following expression for the ionisation single differential cross section (ionisation SDCS), $\mathrm{d}\Lambda_{\text{ionis}}/\mathrm{d}W$, or inverse mean free path, for the ejection of an electron with kinetic energy W:

$$\frac{\mathrm{d}\Lambda_{\text{ionis}}(T, W, q)}{\mathrm{d}W} = \frac{e^2}{\pi\hbar^2}\frac{M_1}{T}\int_{\kappa_-}^{\kappa_+}\frac{\mathrm{d}k}{k}[Z_1 - \rho_q(k)]^2\mathrm{Im}\left[\frac{-1}{\varepsilon(k, W + \overline{B})}\right]_{\text{outer}} + \frac{e^2}{\pi\hbar^2}\frac{M_1}{T}\sum_j \alpha_j \sum_{n\ell}\int_{K_-}^{K_+}\frac{\mathrm{d}k}{k}[Z_1 - \rho_q(k)]^2\mathrm{Im}\left[\frac{-1}{\varepsilon(k, W + B^j_{\text{ionis},n\ell})}\right]_{\text{inner},j,n\ell}, \tag{30}$$

where $\kappa_\pm = (\sqrt{2M_1}/\hbar)(\sqrt{T} \pm \sqrt{T - W - \overline{B}})$, $K_\pm = (\sqrt{2M_1}/\hbar)(\sqrt{T} \pm \sqrt{T - W - B^j_{\text{ionis},n\ell}})$, and α_j is the stoichiometry coefficient of each element j. Note that the key quantity to compute the ionisation cross section is the target ELF over the whole energy and momentum transfer, which is calculated by the MELF-GOS methodology (Sect. 2.1.1). So once the optical ELF of the target is known experimentally, the many-body interactions and the physical-state effects are naturally included in the subsequent calculations.

The mean binding energy of the target outer-shell electrons, $\overline{B}$, can be estimated from quantum chemistry calculations [99] for any biological media. Assuming a simple average of the binding energies of the outer-shell orbitals, the value for liquid water was set to 18.13 eV [94, 96], while for organic compounds it was assumed to be ∼20 eV [98]. However, it is well known that the outer the shell is, the larger contribution to the ionisation cross section has. For this reason, we have re-estimated these energies, according to this fact, to be 13 eV for liquid water and ∼ 15 eV for the rest of the biomaterials [100], and these are the values used for this work. The significance of this model lies in the possibility to calculate several radiological quantities such as single and total ionisation cross sections, as well as the number or the average energy of the emitted electrons, for any swift projectiles travelling in condensed biological targets, such as liquid water, DNA and its components, proteins, lipids, carbohydrates or cell constituents. It has been found that this approximation yields good results in comparison with available experimental data [94, 98, 101].

With the information obtained in the preceding paragraph, we can estimate the production of secondary electrons and its energy distribution along the whole Bragg curve, paying especial attention to depths around the Bragg peak, where the maximum energy deposition takes place. As we have presented in Sect. 4.3, an initial monoenergetic proton beam travelling through a medium, due to the stochastic inelastic interactions and the cumulative effect of the energy-loss straggling, develops a broad energy distribution, which depends on the initial proton energy and the travelled depth. In order to find realistic energy distributions of the secondary electrons generated by the projectile impact it is necessary to take into account the energy distribution of the proton beam, which can be reliably simulated by the SEICS code.

Once the energy distribution $\mathrm{d}N(T_0, z, T, q)/\mathrm{d}T$ at a depth z of the projectiles with charge q and initial kinetic energy T_0 is known, the realistic production of secondary electrons at any depth z generated by the proton beam must be calculated as a convolution between the ionisation inverse mean free path for a given energy T of the proton $\mathrm{d}\Lambda_{\mathrm{ionis}}(T, W, q)/\mathrm{d}W$ (see Eq. (30)), and the energy distribution of the beam, namely:

$$\frac{\mathrm{d}\Lambda^{\mathrm{conv}}_{\mathrm{ionis}}(T_0, z, W)}{\mathrm{d}W} = \frac{1}{N_0}\int_0^{T_0} \mathrm{d}T \sum_{q=0}^{Z_1} \frac{\mathrm{d}N(T_0, z, T, q)}{\mathrm{d}T} \frac{\mathrm{d}\Lambda_{\mathrm{ionis}}(T, W, q)}{\mathrm{d}W}\,, \qquad (31)$$

where N_0 is the initial number of projectiles that bombard the target. A summation over all the charge states q must be performed to account for all the possible projectiles that can ionise the target.

In Fig. 12 we show the convoluted differential (in energy) ionisation cross section $\mathrm{d}\Lambda^{\mathrm{conv}}_{\mathrm{ionis}}(T_0, z, W)/\mathrm{d}W$ for a proton beam incident on liquid water with an initial energy $T_0 = 150$ MeV, as a function of the energy W of the emitted electrons and at depths z around the Bragg peak. The number of ejected electrons qualitatively follows the shape of the depth-dose curve, that is, the ionisation yield reaches a maximum at the Bragg peak (see Fig. 4). It is worth to notice that at each depth, the maximum number of secondary electrons is emitted at low energies, around 10 eV,

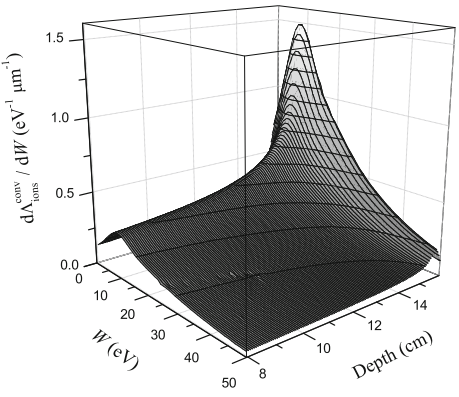

Fig. 12 Energy spectrum of secondary electrons generated by a 150 MeV proton beam in liquid water, as a function of the depth and the electron kinetic energy W. This result has been obtained from the convolution of the ionisation cross section and the proton energy distribution at each depth

with a sizeable increase in the Bragg peak region. This is particularly noteworthy due to the especial role played by low energy electrons in cellular damage [31, 32].

We analyse in more detail these convoluted energy distributions at the Bragg peak, $z_{\max}$, in Fig. 13 for several relevant biomolecules. Curves in Fig. 13(a) show the SDCS for ionisation of liquid water by a proton beam incident with $T_0 = 150$ MeV, obtained by convolution with the proton energy distribution at $z_{\max}$ (solid line), as explained

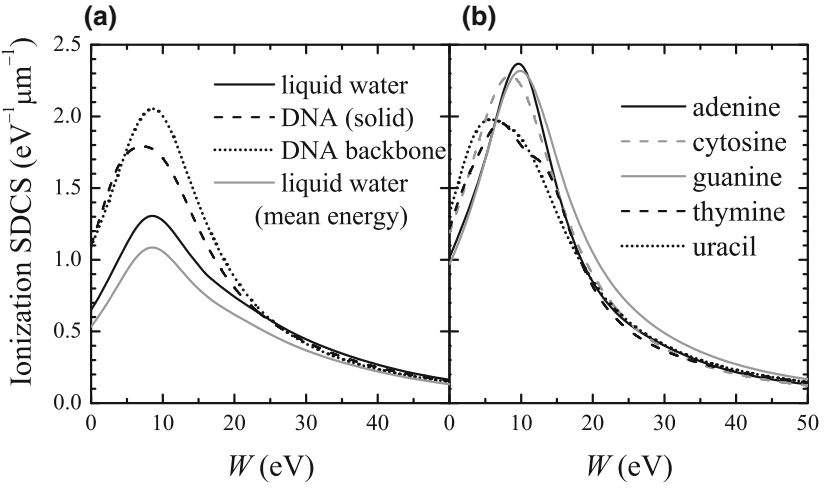

Fig. 13 **a** Convoluted energy distributions of secondary electrons (see text for more details), as a function of their ejection energy W, produced at the depth $z_{\max}$ corresponding to the Bragg peak by a 150 MeV proton beam incident on liquid water (*solid line*), DNA (*dashed line*) and backbone (*dotted line*); for comparison purposes, the energy distribution in liquid water obtained from the mean energy of the proton beam at the Bragg peak is also depicted (*grey solid line*). **b** Convoluted energy distributions of secondary electrons produced by at the Bragg peak by a 150 MeV proton beam in liquid water, but now considering that they are generated by adenide (*solid line*), cytosine (*grey dashed line*), guanine (*grey solid line*), thymine (*dashed line*) and uracil (*dotted line*)

previously, or when only considering the mean energy $\langle T \rangle$ of the beam at that depth (grey solid line). It can be seen that taking into account the energy spectrum of the protons increases the number of ejected secondary electrons in ∼20 % with respect to the mean proton energy calculation. This behaviour comes from the increased ionisation SDCS for the low energy protons [94] that appear in the distribution at Bragg peak.

Thus, the low energy tail of the proton energy distribution at each depth contributes largely to the ionisation SDCS. As low energy electrons are known to have an essential role in the damage of biological media due to dissociative electron attachment processes [31], a precise knowledge of the number and energy of the emitted electrons generated by the incidence of energetic ion beams in the biomaterials is of major relevance. Hence, it is indispensable to link the data obtained with the SEICS code for the energy distribution of the projectile at each depth with the energy distribution of the secondary electrons at each projectile energy in order to obtain accurate values for the initial conditions of the energy spectra, for the purpose of track-structure simulations of secondary electron transport. For these purposes, an increase of 20 % in the number of produced electrons might have noticeable consequences.

Figure 13a also depicts the ionisation SDCS for protons in DNA and its backbone calculated following the convolution method previously outlined, considering that the proton beam has been slowed down in liquid water. Although the Bragg curve is calculated in liquid water (the main medium where the incident projectiles propagate), the ionisation SDCS are obtained replacing at the Bragg peak depth the dielectric properties of liquid water by those of a different biological material, in order to determine the effect of the target composition on the electron production, which will determine the microscopic track-structure. The dashed and dotted lines in Fig. 13b correspond to the replacement of liquid water by solid DNA [102] and by the DNA sugar-phosphate backbone [99], respectively. The results for the rest of DNA/RNA bases (adenine, cytosine, guanine, thymine, and uracil) are shown by different lines in Fig. 13b. Their atomic compositions and densities can be found in Ref. [94]; however, here we have used a density of 1.35 g/cm^3 for the backbone, instead of 1 g/cm^3, to coincide with the DNA density. As it can be clearly seen, all the DNA/RNA components present a convoluted ionisation SDCS that is between 35 and 80 % larger than liquid water. This result indicates that the electron production can be substantially higher in a realistic biological target (e.g., cell nucleus) as compared to pure liquid water, which is currently used as a universal biological surrogate. In addition, the different molecular components of DNA/RNA could present somewhat different ionisation probabilities, although within a certain range, as it can be observed from the figure.

5 Summary and Conclusions

In this chapter, we have presented an overview of the procedures and results that can be obtained through a detailed simulation study of the propagation, energy deposition

and electron production of energetic proton beams in materials of radiotherapeutic interest, especially liquid water. The outcomes of these simulations are relevant for ion beam cancer therapy purposes.

The study is conducted by using the SEICS code (Simulation of Energetic Ions and Clusters through Solids), which combines the Monte Carlo and Molecular Dynamics techniques to follow the motion of energetic ions through condensed matter. The main characteristics of SEICS have been explained in Sect. 2, where the procedure for treating the most relevant interactions between energetic protons and a condensed biological target have been featured, namely, electronic excitations, multiple elastic scattering, electron capture and loss, and nuclear fragmentation reactions.

The main interaction channel, affecting both the position and shape of the Bragg peak, i.e., the electronic excitation process, has been reviewed in Sect. 2.1. We have explained the main features of the dielectric formalism and the MELF-GOS method, which is particularly well suited for calculating the relevant electronic energy loss quantities in condensed matter (i.e., taking into account chemical and phase effects of the target). It has been shown how this methodology is capable of perfectly reproducing the experimental electronic excitation spectrum of liquid water reported in Refs. [54, 55]. The calculated stopping power of liquid water for proton beams has been compared to the available experimental data for liquid and solid water, finding a general good agreement.

The shape of the Bragg peak is also affected by the nuclear fragmentation reactions. We have implemented a simple method that incorporates this inelastic interaction into the simulation, based on the cross sections provided in Ref. [76], as explained in Sect. 2.4. The method accounts for the loss of primary protons according to the total nuclear cross sections, and then the residual energy of the charged secondary particles (protons and heavier ions) that are produced in the reaction is deposited locally.

Before applying the SEICS code, having as the main input the energy loss quantities calculated for liquid water with the dielectric formalism, to problems related to ion beam cancer therapy, we have benchmarked both of them (the code and the electronic energy loss) against experimental data in Sect. 3. Our simulations have reproduced the experimental energy distributions obtained at several angles when a 2 MeV proton beam irradiates a thin liquid water jet [29, 30]. We have found that it is possible to perfectly reproduce the experimental proton energy spectra by only reducing the jet diameter to 48.25 μm (3.5 % reduction compared to the nominal 50 μm diameter). Such a reduction is plausible, assuming a possible evaporation of the liquid water jet into vacuum. Therefore, we conclude that our calculated stopping power for protons in liquid water is accurate, and that the SEICS code works appropriately, so it can be used for studying problems related to ion beam cancer therapy.

This study has been presented in Sect. 4, where different characteristics of proton beams in liquid water have been discussed. The shape of the depth-dose (i.e., Bragg) curve, and the influence on it of the different interaction processes, was studied in Sect. 4.1. We showed how the stopping power determined the position of the Bragg peak, whereas the broadening of its shape was mainly due to the energy-loss

straggling, with additional contribution from nuclear fragmentation reactions. The implementation of the nuclear fragmentation reactions, with the local energy deposition approximation, was checked against experimental data, finding a satisfactory agreement.

Regarding the multiple elastic scattering, it was shown to be responsible of the projectiles deviation from their initial direction, leading to the transversal dispersion of the beam, which results in a lateral spreading of the dose profile. We have studied this aspect in Sect. 4.2, where the root mean square radius of the transversal section of the proton beam has been studied in liquid water for different initial energies. We have found that it can be parameterised as a function of the incident energy, providing the corresponding parameters, which allows the calculation of the lateral dose analytically.

In Sect. 4.3, we have studied how the energy of the proton beam evolves along the Bragg curve. Due to the energy-loss straggling, the initially monoenergetic proton beam develops an energy distribution, which becomes rather wide at the Bragg peak depth. At this position, the mean energy of the distribution and the full width at half maximum are 10 % of the initial beam energy, as we have found from several simulations.

This distribution of the proton energy can affect the number and energy of secondary electrons produced at each depth, which has been studied in Sect. 4.4. The energy spectra of secondary electrons generated by a proton with a given energy, as calculated with the dielectric formalism, have been convoluted with the energy distributions of the primary protons, to produce realistic energy spectra of secondary electrons produced at each depth in the target. They have been compared with the spectra obtained when using instead the mean energy of the proton beam. The former (and more realistic) procedure leads to an increase of $\sim$20 % in the number of secondary electrons, compared to the latter. Finally, we have also calculated the ionisation single differential cross section for liquid water and other biological targets, namely DNA and its molecular components, i.e., the five DNA/RNA bases (adenine, cytosine, guanine, thymine, and uracil) and the sugar-phosphate backbone. By comparing these values, we have demonstrated that all these biomolecules present larger ionisation probabilities than liquid water. This is an important result for further studies of biodamage mechanisms at the nano- and microscale, which are largely related to the energy and number of electrons produced and propagating in realistic cellular components.

Acknowledgements Illuminating and fruitful discussions with many collaborators are acknowledged. Most of the research presented in this paper was developed under the warm and stimulating atmosphere of the COST Action MP 1002, Nanoscale Insights into Ion Beam Cancer Therapy. During the last revision of this work we heard of the death of Helmut Paul, an excellent friend and a better scientist, to whom we dedicate this work. We thank partial financial support by the Spanish Ministerio de Economía y Competitividad (Project FIS2014-58849-P) and the Murcia Regional Agency of Science and Technology (project 19907/GERM/15). PdV acknowledges financial support from the European Union's FP7-People Program (Marie Curie Actions) within the Initial Training Network No. 608163 "ARGENT".

References

1. Löeffler JS, Durante M (2013) Charged particle therapy-optimization, challenges and future directions. Nat Rev Clin Oncol 10:411–424
2. PTCOG: Particle Therapy Co-Operative Group webpage. http://www.ptcog.ch/
3. Sigmund P (2006) Particle penetration and radiation effects. Springer-Verlag, Berlin
4. Paul H (2007) The mean ionization potential of water, and its connection to the range of energetic carbon ions in water. Nucl Instr Meth B 255:435–437
5. Besemer A, Paganetti H, Bednarz B (2013) The clinical impact of uncertainties in the mean excitation energy of human tissues during proton therapy. Phys Med Biol 58:887–902
6. Surdutovich E, Solov'yov AV (2014) Multiscale approach to the physics of radiation damage with ions. Eur Phys J D 68:353
7. Uehara S, Nikjoo H, Goodhead DT (1992) Cross-sections for water vapour for the Monte Carlo electron track structure code from 10 eV to the MeV region. Phys Med Biol 37:1841–1858
8. Friedland W, Dingfelder M, Kundrát P, Jacob P (2011) Track structures, DNA targets and radiation effects in the biophysical Monte Carlo simulation code PARTRAC. Mutation Res 711:28–40
9. Pimblott SM, Mozumder A (1991) Structure of electron tracks in water. 2. Distribution of primary ionizations and excitations in water radiolysis. J Phys Chem 95:7291–7300
10. Nikjoo H, Uehara S, Emfietzoglou D (2012) Interaction of radiation with matter. CRC Press, Boca Raton
11. Champion C, Le Loirec C, Stosic B (2012) EPOTRAN: a full-differential Monte Carlo code for electron and positron transport in liquid and gaseous water. Int J Radiat Biol 88:54–61
12. Böhlen TT, Cerutti F, Chin MPW, Fassò A, Ferrari A, Ortega PG, Mairani A, Sala PR, Smirnov G, Vlachoudis V (2014) The FLUKA Code: developments and challenges for high energy and medical applications. Nucl Data Sheets 120:211–214
13. Waters LS (ed.) (2002) MCNPX User's manual Version 2.3.0. Report LA-UR-02-2607. Los Alamos Nat. Lab., Los Alamos, USA
14. Ziegler JF, Biersack JP, Ziegler MD (2008) SRIM—The stopping and range of ions in matter. SRIM Co., Chester, Maryland
15. Salvat F, Fernández-Varea JM, Sempau J (2011) PENELOPE-2011: a code system for monte carlo simulation of electron and photon transport. OECD NEA Data Bank/NSC DOC(2011)/5 (2011)
16. Agostinelli S, Allison J, Amako K, Apostolakis J, Araujo H, Arce P, Asai M, Axen D, Banerjee S, Barrand G, Behner F, Bellagamba L, Boudreau J, Broglia L, Brunengo A, Burkhardt H et al (2003) GEANT4-a simulation toolkit. Nucl Instrum Methods Phys Res A 506:250–303
17. Nikjoo H, Uehara S, Emfietzoglou D, Cucinotta F (2006) Track-structure codes in radiation research. Radiat Meas 41:1052–1074
18. Incerti S, Baldacchino G, Bernal M, Capra R, Champion C, Francis Z, Guatelli S, Gueye P, Mantero A, Mascialino B, Moretto P, Nieminen P, Rosenfeld A, Villagrasa C, Zacharatou C (2010) The GEANT4-DNA project. Int J Model Simul Sci Comput 1:157
19. Muñoz A, Perez J, Garcia G, Blanco F (2005) An approach to Monte Carlo simulation of low-energy electron and photon interactions in air. Nucl Instrum Methods Phys Res A 536:176–188
20. Muñoz A, Fuss MC, Cortés-Giraldo MA, Incerti S, Ivanchenko V, Ivanchenko A, Quesada JM, Salvat F, Champion C, García Gómez-Tejedor G (2012) In: García Gómez-Tejedor G (ed.) Radiation damage in biomolecular systems, Chap. 13. Springer, Dordrecht
21. Garcia-Molina R, Abril I, Heredia-Avalos S, Kyriakou I, Emfietzoglou D (2011) A combined molecular dynamics and Monte Carlo simulation of the spatial distribution of energy deposition by proton beams in liquid water. Phys Med Biol 56:6475–6493
22. Lindhard J (1954) On the properties of a gas of charged particles. K Dan Vidensk Selsk Mat.-Fys Medd 28(8):1
23. Garcia-Molina R, Abril I, Denton CD, Heredia-Avalos S, Kyriakou I, Emfietzoglou D (2009) Calculated depth-dose distributions for H^+ and He^+ beams in liquid water. Nucl Instrum Meth Phys Res B 267:2647–2652

24. Limandri S, de Vera P, Fadanelli RC, Nagamine LCCM, Mello A, Garcia-Molina R, Behar M, Abril I (2014) Energy deposition of H and He ion beams in hydroxyapatite films: a study with implications for ion-beam cancer therapy. Phys Rev E 89:022703
25. Abril I, Garcia-Molina R, Denton CD, Kyriakou I, Emfietzoglou D (2011) Energy loss of hydrogen- and helium-ion beams in DNA: calculations based on a realistic energy-loss function of the target. Rad Res 175:247–255
26. de Vera P, Abril I, Garcia-Molina R (2011) Inelastic scattering of electron and light ion beams in organic polymers. J Appl Phys 109:094901
27. Garcia-Molina R, Abril I, de Vera P, Kyriakou I, Emfietzoglou D (2014) A study of the energy deposition profile of proton beams in materials of hadron therapeutic interest. Appl Radiat Isotopes 83:109–114
28. Abril I, Garcia-Molina R, de Vera P, Kyriakou I, Emfietzoglou D (2013) Inelastic collisions of energetic protons in biological media. Adv Quantum Chem 65:129–164
29. Shimizu M, Kaneda M, Hayakawa T, Tsuchida H, Itoh A (2009) Stopping cross sections of liquid water for MeV energy protons. Nucl Instrum Meth Phys Res B 267:2667–2670
30. Shimizu M, Hayakawa T, Kaneda M, Tsuchida H, Itoh A (2010) Stopping cross-sections of liquid water for 0.3-2.0 MeV protons. Vacuum 84:1002–1004
31. Boudaïffa B, Cloutier P, Hunting D, Huels MA, Sanche L (2000) Resonant formation of DNA strand breaks by low-energy (3 to 20 eV) electrons. Science 287:1658–1660
32. Rezaee M, Cloutier P, Bass AD, Michaud M, Hunting DJ, Sanche L (2012) Absolute cross section for low-energy-electron damage to condensed macromolecules: a case study of DNA. Phys Rev E 86:031913
33. Garcia-Molina R, Denton CD, Abril I, Arista NR (2000) Energy-loss and exit-angle distributions of fragmented H_2^+ ions after traversing carbon foils. Phys Rev A 62(1):012901
34. Heredia-Avalos S, Garcia-Molina R, Abril I (2007) Energy-loss calculation of swift C_n^+ ($n =$ 2-60) clusters through thin foils. Phys Rev A 76:012901
35. Garcia-Molina R, Abril I, de Vera P, Kyriakou I, Emfietzoglou D (2012) In: Belkić D (ed) Fast ion-atom and ion-molecule collisions. World Scientific Publishing Company, Singapore
36. Allen MP, Tildesley DJ (1989) Computer simulation of liquids. Oxford University Press, Oxford
37. Box GEP, Müller ME (1958) A note on the generation of random normal deviates. Ann Math Stat 29:610–611
38. Press WH, Teukolsky SA, Vetterling WT, Flannery BP (1997) Numerical recipes in Fortran 77. The art of scientific computing, 2nd edn. Cambridge University Press, Cambridge
39. Abril I, Garcia-Molina R, Denton CD, Pérez-Pérez F, Arista NR (1998) Dielectric description of wakes and stopping powers in solids. Phys Rev A 58:357–366
40. Heredia-Avalos S, Garcia-Molina R, Fernández-Varea JM, Abril I (2005) Calculated energy loss of swift He, Li, B, and N ions in SiO_2, Al_2O_3, and ZrO_2. Phys Rev A 72:052902
41. Garcia-Molina R, Abril I, Kyriakou I, Emfietzoglou D (2012) Energy loss of swift protons in liquid water: role of optical data input and extension algorithms. In: García Gómez-Tejedor G, Fuss MC (eds) Radiation damage in biomolecular systems, Chap. 15. Springer, Dordrecht
42. Inokuti M (1971) Inelastic collisions of fast charged particles with atoms and molecules—The Bethe theory revisited. Rev Mod Phys 43:297–347
43. Fano U (1963) Penetration of protons, alpha particles, and mesons. Ann Rev Nucl Sci 13:1–66
44. de Vera P, Abril I, Garcia-Molina R (2014) Water equivalent properties of materials commonly used in proton dosimetry. Appl Radiat Isotopes 83:122–127
45. Fermi E (1940) The ionization loss of energy in gases and in condensed materials. Phys Rev 57:485
46. Ritchie RH, Howie A (1977) Electron excitation and the optical potential in electron microscopy. Phil Mag 36:463–481
47. Brandt W, Kitagawa M Effective stopping-power charges of swift ions in condensed matter. Phys Rev B 25:5631
48. Denton CD, Abril I, Garcia-Molina R, Moreno-Marín JC, Heredia-Avalos S (2008) Influence of the description of the target energy-loss function on the energy loss of swift projectiles. Surf Interface Anal 40:1481–1487

49. Mermin ND (1970) Lindhard dielectric function in the relaxation-time approximation. Phys Rev B 1:2362–2362
50. Egerton RF (2011) Electron energy-loss spectroscopy in the electron microscope, 3rd edn. Springer, New York
51. Bragg WH, Kleeman R (1905) On the alpha particles of radium, and their loss of range in passing through various atoms and molecules. Phil Magaz Series 10:318–340
52. Pines D (1999) Elementary excitations in solids. Perseus Books, Urbana, Illinois
53. Dressel M, Grüner G (2002) Electrodynamics of solids. Optical properties of electrons in matter. Cambridge University Press, Cambridge
54. Watanabe N, Hayashi H, Udagawa Y (1997) Bethe surface of liquid water determined by inelastic X-ray scattering spectroscopy and electron correlation effects. Bull Chem Soc Jpn 70:719–726
55. Hayashi H, Watanabe N, Udagawa Y, Kao C (2000) The complete optical spectrum of liquid water measured by inelastic x-ray scattering. Proc Nat Academy Sci USA 97:6264–6266
56. Garcia-Molina R, Abril I, Denton CD, Heredia-Avalos S (2006) Allotropic effects on the energy loss of swift H^+ and He^+ ion beams through thin foils. Nucl Instrum Meth Phys Res B 249:6–12
57. Abril I, Moreno-Marín JC, Fernández-Varea JM, Denton CD, Heredia-Avalos S, Garcia-Molina R (2007) Calculation of the energy loss of swift H and He ions in Ag using the dielectric formalism: the role of inner-shell ionization. Nucl Instrum Meth Phys Res B 256:172–176
58. Heredia-Avalos S, Abril I, Denton CD, Moreno-Marín JC, Garcia-Molina R (2007) Target inner-shells contributions to the stopping power and straggling for H and He ions in gold. J Phys Conden Matter 19:466205
59. Montanari C, Miraglia J, Heredia-Avalos S, Garcia-Molina R, Abril I (2007) Calculation of energy-loss straggling of C, Al, Si, and Cu for fast H, He, and Li ions. Phys Rev A 75:022903
60. Abril I, Behar M, Garcia-Molina R, Fadanelli RC, Nagamine LC, Grande PL, Schünemann L, Denton CD, Arista NR, Saitovitch EB (2009) Experimental and theoretical studies of the energy-loss straggling of H and He ion beams in HfO_2 films. Eur Phys J D 54:65–70
61. Behar M, Fadanelli RC, Abril I, Garcia-Molina R, Denton CD, Nagamine LCCM, Arista NR (2009) Energy loss of proton, α particle, and electron beams in hafnium dioxide films. Phys Rev A 80:062901
62. Behar M, Denton CD, Fadanelli RC, Abril I, Cantero ED, Garcia-Molina R, Nagamine LCC (2010) Experimental and theoretical determination of the stopping power of ZrO_2 films for protons and α-particles. Eur Phys J D 59:209–213
63. Limandri SP, Fadanelli RC, Behar M, Nagamine LCCM. Fernández-Varea JM, Abril I, Garcia-Molina R, Montanari CC, Aguiar JC, Mitnik D, Miraglia JE, Arista NR (2014) Stopping cross sections of TiO_2 for H and He ions. Eur Phys J D 68:194-1–8
64. Fadanelli RC, Behar M, Nagamine LCCM, Vos M, Arista NR, Nascimento CD, Garcia-Molina R, Abril I (2015) Energy loss function of solids assessed by ion beam energy-loss measurements: practical application to Ta_2O_5. J Phys Chem C 119:20561–20570
65. Garcia-Molina R, Abril I, Kyriakou I, Emfietzoglou D (2016) Inelastic scattering and energy loss of swift electron beams in biologically relevant materials. Surf Interf Anal. doi:10.1002/sia.5947
66. Schiwietz G, Grande PL (2001) Improved charge-state formulas. Nucl Instrum Meth Phys Res B 175–177:125–131
67. Siiskonen T, Kettunen H, Peräjärvi K, Javanainen A, Rossi M, Trzaska WH, Turunen J, Virtanen A (2011) Energy loss measurement of protons in liquid water. Phys Med Biol 56:2367–2374
68. Wenzel WA, Whaling W (1952) The stopping cross section of D_2O ice. Phys Rev 87:499–503
69. Andrews DA, Newton G (1977) The stopping power of heavy ice for low-energy (10–30 keV) deuterons. J Phys D 10:845–850
70. Bauer P, Kaferbock W, Necas V (1994) Investigation of the electronic energy loss of hydrogen ions in H_2O: influence of the state of aggregation. Nucl Instrum Meth Phys Res B 93:132–136

71. ICRU, Report 49 (1993) Stopping powers and ranges for protons and alpha particles. International Commission on Radiation Units and Measurements, Bethesda, Maryland
72. Möller W, Pospiech G, Schrieder G (1975) Multiple scattering calculations on ions passing through thin amorphous foils. Nucl Instrum Meth Phys Res B 130:265–270
73. Zajfman D, Both G, Kanter EP, Vager Z (1990) Multiple scattering of MeV atomic and molecular ions traversing ultrathin films. Phys Rev A 41:2482–2488
74. Turner JE, Wright HA, Hamm RN (1985) A Monte Carlo primer for health physicists. Health Phys 48:717–733
75. Brandt W, Sizmann R (1975) In: Datz S, Appleton BR, Moak CD (eds.) Atomic collisions in solids. Plenum Press, New York
76. ICRU (2000) Report 63. Nuclear data for neutron and proton radiotherapy and for radiation protection. International Commission on Radiation Units and Measurements, Bethesda, Maryland
77. Medin J, Andreo P (1997) Monte Carlo calculated stopping-power ratios, water/air, for clinical proton dosimetry (50–250 MeV). Phys Med Biol 42:89–106
78. Paul H (2010) Recent results in stopping power for positive ions, and some critical comments. Nucl Instrum Meth Phys Res B 268:3421–3425
79. Paul H (2013) On the accuracy of stopping power codes and ion ranges used for hadron therapy. Adv Quantum Chem 65:39–62
80. Garcia-Molina R, Abril I, de Vera P, Kyriakou I, Emfietzoglou D (2012) Role of the interaction processes in the depth-dose distribution of proton beams in liquid water. J Phys Confer Series 373:012015
81. Paganetti H (2012) Range uncertainties in proton therapy and the role of Monte Carlo simulations. Phys Med Biol 57:R99–R117
82. Zhang X, Liu W, Li Y, Li X, Quan M, Mohan R, Anand A, Sahoo N, Gillin M, Zhu XR (2011) Parameterization of multiple Bragg curves for scanning proton beams using simultaneous fitting of multiple curves. Phys Med Biol 56:7725–7735
83. Kundrát P (2007) A semi-analytical radiobiological model may assist treatment planning in light ion radiotherapy. Phys Med Biol 52:6813–6830
84. Abril I, de Vera P, Garcia-Molina R, Kyriakou I, Emfietzoglou D (2015) Lateral spread of dose distribution by therapeutic proton beams in liquid water. Nucl Instrum Meth Phys Res B 352:176–180
85. Kraft G (1990) The radiobiological and physical basis for radiotherapy with protons and heavier ions. Strahlenther Onkol 166:10–13
86. Hollmark M, Uhrdin J, Belkić D, Gudowska I, Brahme A (2004) Influence of multiple scattering and energy loss straggling on the absorbed dose distributions of therapeutic light ion beams: I. Analytical pencil beam model. Phys Med Biol 49:3247–3265
87. Solov'yov AV, Surdutovich E, Scifoni E, Mishustin I, Greiner W (2009) Physics of ion beam cancer therapy: a multiscale approach. Phys Rev E 79:011909
88. Scholz M, Kraft G (1996) Track structure and the calculation of biological effects of heavy charged particles. Adv Space Res 18:5–14
89. Schardt D, Elsässer T, Schulz-Ertner D (2010) Heavy-ion tumor therapy: physical and radiobiological benefits. Rev Modern Phys 82:383–425
90. Pan X, Cloutier P, Hunting D, Sanche L (2003) Dissociative electron attachment to DNA. Phys Rev Lett 90:208102
91. Rudd ME, Kim YK (1992) Electron production in proton collisions with atoms and molecules: energy distributions. Rev Modern Phys 64:441–490
92. Vriens L (1967) Binary-encounter proton-atom collision theory. Proc Phys Soc London 90:935–944
93. ICRU (1996) Report 55. Secondary electron spectra from charged particle interactions. International Commission on Radiation Units and Measurements, Bethesda, Maryland
94. de Vera P, Garcia-Molina R, Abril I, Solov'yov AV (2013) Semiempirical model for the ion impact ionization of complex biological media. Phys Rev Lett 110:148104

95. de Vera P, Garcia-Molina R, Abril I (2015) Angular and energy distributions of electrons produced in arbitrary biomaterials by proton impact. Phys Rev Lett 114:018101
96. Dingfelder M, Hantke D, Inokuti M, Paretzke HG (1998) Electron inelastic-scattering cross sections in liquid water. Radiat Phys Chem 53:1–18
97. Emfietzoglou D, Moscovitch M (2003) Secondary electron spectra for fast proton impact on gaseous and liquid water. Nucl Instrum Meth Phys Res B 209:239–245
98. de Vera P, Abril I, Garcia-Molina R, Solov'yov AV (2013) Ionization of biomolecular targets by ion impact: input data for radiobiological applications. J Phys Conf Series 438:012015
99. Bernhardt P, Paretzke HG (2003) Calculation of electron impact ionization cross sections of DNA using the Deutsch-Mark and Binary-Encounter-Bethe formalisms. Int J Mass Spectrom 224:599–611
100. de Vera P, Garcia-Molina R, Abril I: To be published
101. Wang M, Rudek B, Bennett D, de Vera P, Bug M, Buhr T, Baek WY, Hilgers G, Rabus H (2016) Cross sections for ionization of tetrahydrofuran by protons at energies between 300 and 3000 keV. Phys Rev A 93:052711-1–16
102. Inagaki T, Hamm RN, Arakawa ET, Painter LR (1974) Optical and dielectric properties of DNA in the extreme ultraviolet. J Chem Phys 61:4246–4250

http://www.springer.com/978-3-319-43028-7

Nanoscale Insights into Ion-Beam Cancer Therapy
Solov'yov, A. (Ed.)
2017, XX, 498 p. 183 illus., 159 illus. in color.,
Hardcover
ISBN: 978-3-319-43028-7